Disturbed NO signalling gives rise to congenital bicuspid aortic valve and aortopathy.

Authors:

Joshua C. Peterson[1], Lambertus J. Wisse[1], Valerie Wirokromo[1], Tessa van Herwaarden[3], Anke M. Smits[3] PhD, Adriana C. Gittenberger-de Groot[2] PhD, Marie-José T.H. Goumans[3] PhD, J. Conny VanMunsteren[1], Monique R.M. Jongbloed[1, 2] MD PhD, Marco C. DeRuiter[1,×] PhD

Departments and institutions:

[1] Dept. Anatomy and Embryology, Leiden University Medical Center, Leiden, The Netherlands.

[2] Dept. Cardiology, Leiden University Medical Center, Leiden, The Netherlands.

[3] Dept. Chemical Cell Biology, Leiden University Medical Center, Leiden, The Netherlands.

Address for correspondence:

× Corresponding author: Marco C. DeRuiter, PhD

Dept. Anatomy and Embryology, Leiden University Medical Center, PO-Box 9600, 2300RC Leiden, The Netherlands, Email: m.c.deruiter@lumc.nl, Telephone: +31.71.52.69308

Disease Models & Mechanisms • DMM • Accepted manuscript

Summary statement:

NO defects link BAV and aortopathy by inhibition of elastic fibre formation in vascular smooth muscle cells within the ascending aorta of Nos3$^{-/-}$ mice.

Abstract:

Patients with a congenital bicuspid aortic valve (BAV), a valve with two instead of three aortic leaflets, have an increased risk of developing thoracic aneurysms and aortic dissection. The mechanisms underlying BAV-associated aortopathy are poorly understood. This study examined BAV-associated aortopathy in *Nos3*$^{-/-}$ mice, a model with congenital BAV formation. A combination of histological examination and in-vivo ultrasound imaging was used to investigate aortic dilation and dissections in *Nos3*$^{-/-}$ mice. Moreover, cell lineage analysis and single cell RNA sequencing were used to observe the molecular anomalies within vascular smooth muscle cells (VSMCs) of *Nos3*$^{-/-}$ mice. Spontaneous aortic dissections was found in ascending aortas located at the sinotubular junction in ~13% of *Nos3*$^{-/-}$ mice. Moreover, *Nos3*$^{-/-}$ mice were prone to develop aortic dilations in the mid- and distal-ascending aorta during early adulthood. Lower volumes of elastic fibres were found within vessel walls of the ascending aortas of *Nos3*$^{-/-}$ mice as well as incomplete coverage of the aortic inner media by neural crest (NCC)-derived VSMCs. VSMCs of *Nos3*$^{-/-}$ showed downregulation of 15 genes of which 7 were associated with aortic aneurysms and dissections in the human population. Elastin mRNA was most markedly downregulated, followed by Fibulin-5 expression, both primary components of elastic fibres. This study demonstrates that disrupted endothelial mediated NO signalling in mice causes next to a congenital BAV also aortic dilation and dissection as a consequence of inhibited elastic fibre formation in VSMCs within the ascending aorta of *Nos3*$^{-/-}$ mice.

Keywords:

NOS3, Aortic Dissection, Bicuspid Aortic Valve, Nitric Oxide, Development, Congenital Heart Disease

Abbreviations:

AoDd:	Aortic diameter during diastole
AoDs:	Aortic diameter during systole
BAV:	Bicuspid aortic valve
ECM:	Extracellular matrix
HE:	Mayer's Hematoxylin-Eosin
NCC:	Neural crest cell
NO:	Nitric Oxide
RF:	Weigert's Resorcin-Fuchsin
TAV:	Tricuspid aortic valve
VSMC:	Vascular smooth muscle cell

Introduction

Patients with a congenital bicuspid aortic valve (BAV) often develop subsequent aortopathy later in adulthood. Clinical studies show that patients with a BAV have a three-fold increased chance of developing thoracic aortic aneurysms (Cecconi *et al.*, 2006). This aortopathy is considered generally as a haemodynamic result from the disturbed flow caused by the narrowed opening and position of the two leaflets. Various studies demonstrate that first degree relatives of BAV patients with a normal tricuspid aortic valve are at increased risk of developing aortic complications (Biner *et al.*, 2009) indicating that both BAV and aneurysm formation represent a variable phenotypical expression of a common genetic defect (Loscalzo *et al.*, 2007). Remodelling of the extracellular matrix (ECM) has been linked to aortopathy. Patients with aortic aneurysms typically display medial degeneration as a result of elastic fibre fragmentation (Isselbacher, 2005). Moreover, reduced collagen disposition has also been observed in patients with ascending aortic aneurysms (de Figueiredo Borges *et al.*, 2008).

Aortic vasculature and valve development are closely related and share common embryonic cell populations. Endothelial cells populating the arterial pole of the heart also contribute to the outflow tract cushions from which the aortic valve develops through epithelial mesenchymal transition. Cardiac neural crest cells (NCC) and second heart field derived cell populations both contribute to the interstitial cells of the aortic valves and the medial vascular smooth muscle cells (VSMCs) and adventitial fibroblasts of the aorta. Studies using mice have determined anomalies in embryonic cardiac lineages to result in BAV (Laforest, Andelfinger and Nemer, 2011; Peterson *et al.*, 2018), yet much is unknown about how these cell lineages influence ECM composition and contribute to aortic dissections.

In this study, we examined the effects of disrupted NO signalling on the thoracic aorta in *Nos3*$^{-/-}$ mice, which is a genetic BAV model with a ~25% penetrance of the phenotype (Lee *et al.*, 2000; Fernandez *et al.*, 2009; Peterson *et al.*, 2018), to identify developmental processes involved in BAV-associated aortopathy. Understanding early aortic vessel formation is crucial to apprehend the risks involved in aortopathy seen in BAV patients and their tricuspid aortic valve (TAV) relatives.

2. Material and Methods

2.1 Animals

BAV associated aortopathy was studied in aortic tissue of *Nos3*$^{-/-}$ mice and wild type in embryonic and adult stages of development. Mice older than 2 months were considered as adult mice and experiments were performed using a random distribution of male and female mice. The following mice were used in this study: *Nos3*$^{-/-}$ B6.129P2-NOS3tm1Unc/J mice (*purchased from Charles River Laboratories, Maastricht, Netherlands*), B6.Cg-Tg(Wnt1-cre)2Sor/J (*purchased from Jackson laboratories, JAX stock #022501, Bar Harbor, USA*), B6.129(Cg)-Gt(ROSA)26Sortm4(ACTB-tdTomato,-EGFP)Luo/J, (mT/mG) (*purchased from Jackson laboratories, JAX stock # 007576, Bar Harbor, USA). Nos3*$^{-/-}$;*Wnt1Cre;mT/mG*; and *Wnt1Cre;mT/mG* were generated using a cross breeding strategy. All mice were back crossed to the Black6 background using C57BL/6JLumc mice (*purchased from Leiden University Medical Center, Leiden, The Netherlands*).

Embryos were acquired using timed breeding protocols. Adult mice were bred overnight and examined the next morning for the presence of a vaginal plug. In case a plug was observed, embryonic age would be established at (E)0.5 at noon of that day. Embryos were isolated through hysterectomy at E12.5 and E17.5 following dissection in phosphate buffer solution pH 7.4. Genomic DNA was isolated from tail biopsies for genotyping by polymerase chain reaction targeted at *Cre* and *Nos3* according to previous publication (Peterson *et al.*, 2018). All mice were handled according to the Guide for Care and Use of Laboratory Animals, as published by the NIH and experiments were in accordance with relevant local, national and international regulations and guidelines.

2.2 Immunostainings and Histochemistry

Embryos and adult aortic tissues were fixed in 4% paraformaldehyde (0.1M, pH 7.4) for 24h at 4°C and embedded in paraffin. Samples were sectioned serially (5 µm), and mounted on glass slides. Prior to staining, samples were deparaffinized using xylene followed by a series of graded ethanol steps for rehydration into PBS. In case of immunostainings, slides were subjected to microwave antigen retrieval in citric acid buffer (10mM Citric Acid, 0.05% Tween 20 pH = 6.0) for 12 min at 97°C. Sections were incubated with primary antibodies against eGFP (Abcam ab13970), ACTA2 (Sigma-Aldrich A2547) or FBLN5 (Abcam ab202977). Primary antibodies were diluted in PBS-Tween-20 (1/500) with 1% bovine serum albumin (BSA, A8022; Sigma-Aldrich, St. Louis, MO, USA) to avoid non-specific binding. Between subsequent incubation steps all slides were rinsed twice in PBS followed by a single rinse in PBS-Tween-20. Primary antibodies were visualized by incubation with fluorescently labelled

secondary antibodies (Thermo Scientific A-11039), diluted (1/200) in PBS-Tween-20 for 60 min. DAPI (D3571, 1/1000; Life Technologies) was used as a nuclear stain and the slides were mounted with Prolong gold (Life Technologies). Classical histochemistry was used to examine ECM composition. Mayer's Hematoxylin-Eosin (HE) (KLINIPATH VWRK4085-9002) Weigert's Resorcin-Fuchsin (RF) (Sigma-Aldrich 100591), Sirius Red (Sigma-Aldrich 365548) staining were performed according to published protocols (Culling, 1974; Junqueira, Bignolas and Brentani, 1979; Cardiff, Miller and Munn, 2014).

2.3 *In vivo* aortic ultrasound measurements

Wild type (N=8 of which 1 female and 7 males) and *Nos3*$^{-/-}$ (N=4 of which 1 female and 3 males) mice were selected at 4 months of age. Mice were randomized and ultrasound measurements of systolic and diastolic aortic diameters (AoDs and AoDd respectively) as well as data analysis were executed blinded. Aortic diameters were measured perpendicular to the inner curvature. Mice were anesthetized using isoflurane and monitored for temperature and heart rate during ultrasound measurements. Ultrasound images were collected using Vevo3100 (FUJIFILM Visual Sonics, Toronto, ON, Canada) and the MX400, 20–46 MHz probe with a centre frequency of 30 MHz. Sagittal ECG-gated kHz visualization (EKV) were captured for analysis. Data analysis was performed using Vevo LAB 3.2.0 software. Circumferential Green-Lagrange strain was calculated according to previous publication (Goergen *et al.*, 2010) using the following equation:

$$0.5 * \left[\left(\frac{AoDs}{AoDd}\right)^2 - 1\right] * 100\%$$

2.4. Three-dimensional reconstructions

Aortic 3D reconstructions of E12.5 *Nos3*$^{-/-}$*;Wnt1Cre;mTmG* and *Wnt1Cre;mTmG* embryos were made with Amira software 6.3 (Template Graphics Software Inc., Houston, TX, USA). Tissue sections (5 µm) were collected from paraffin embedded embryos and immunostained using anti-eGFP and DAPI. Slides were scanned using the panoramic 250 flash III slide scanner (3DHISTECH Ltd., Budapest, Hungary) and images of identical scale and exposure were exported using Histech Panoramic Viewer (3DHISTECH Ltd., Budapest, Hungary) and aligned in Amira. Relevant cardiac structures were labelled and surface views were exported to PDF format with the Adobe Acrobat 9.5 software package.

2.5. Extracellular matrix quantification

ECM of elastin and collagen were examined in aortic vessel walls of wild type (N=5) and *Nos3*$^{-/-}$ (N=6) mice aged E17.5 as well as in wild type and *Nos3*$^{-/-}$ adult mice (P2 months, N=6 of which 2 females and 4 males, and N=5 of which 3 females and 2 males respectively). Histological sections were scanned using the panoramic 250 flash III slide scanner (3DHISTECH Ltd., Budapest, Hungary). Elastin and collagen was quantified in aortic vessel wall of the proximal-, mid-, and distal-ascending aorta covering a total length of 250 µm and 500 µm in E17.5 and adult mice respectively, corresponding to the same anatomical regions within the aorta. This was achieved with the use of a macro designed in Fiji (Schindelin *et al.*, 2012) which allowed for the quantification of volumetric elastin and collagen respective to the vessel wall. The aortic vessel wall was identified manually in histological images (8-bit RGB) of idential resolution and maginifcation in wild type and *Nos3*$^{-/-}$ mice. Elastin was detected using the following RGB thresholds: Hue (min=169, max=227) Saturation (min=34, max=255), Brightness (min=17, max=185) . Collagen was defined using the following RGB thresholds: Hue (min= 0 max= 255) Saturation (min=0, max=255), Brightness (min=0, max=199).

ECM measurements were presented relative to the volume of aortic vessel wall. Final volumetric calculations were processed in Excel 2016 (Microsoft, Redmond, Washington, USA).

2.6 Survival analysis

Events of spontaneous mortality were recorded in breeding colonies of wild type and *Nos3*$^{-/-}$ mice up to 1 year of age. The number of spontaneous deaths recorded was 103 in wild type colonies and 133 in *Nos3*$^{-/-}$ colonies. Mantel-Cox comparison of survival curves was used to examine the temporal distribution of spontaneous death events between the two groups.

2.7. Neural crest lineage analysis

Neural crest lineage analysis was performed similar to previous publication (Peterson *et al.*, 2018). Briefly, fluorescent images were collected using Leica Sp8 confocal microscopy (Leica Microsystems, Buffalo Grove IL, USA). Measurements were performed on aortic vessel walls from transverse sections (5 µm) of *Wnt1Cre;mTmG* (N=4) and *Nos3*$^{-/-}$*;Wnt1Cre;mTmG* (N=4) for stages E12.5 and E17.5. Of each embryo the proximal-, mid-, and distal-ascending aorta were imaged completely covering a total aortic length of 180 µm and 250 µm in E12.5 and E17.5 embryos respectively, corresponding to the same

anatomical regions within the aorta. The proximal ascending aorta marks the border of the sinotubular junction and the tubular ascending aorta. The distal ascending aorta marks the border in which the tubular ascending aorta transitions into the proximal aortic arch prior to the brachiocephalic artery. The mid ascending aorta is positioned in the middle of the tubular ascending aorta. Image analysis was performed using a macro designed in Fiji (Schindelin *et al.*, 2012). The macro was designed to differentiate the nuclear volume of $Wnt1Cre^{+}$ lineage derived nuclei from the nuclear volume of all $DAPI^{+}$ nuclei within the aortic vessel wall. The regions of the aortic vessel wall were selected manually and $DAPI^{+}$ nuclei found within a body of cytoplasmic GFP were measured as lineage specific nuclei relative to the total volume of $DAPI^{+}$ nuclei in the aortic vessel wall. Image thresholds for GFP^{+} cytoplasm were set at a pixel intensity of 120 and $DAPI^{+}$ thresholds were automatically detected using the imageJ "default" algorithm. Final volumetric calculations were processed in Excel 2016 (Microsoft, Redmond, Washington, USA).

2.8 Cell sorting and single cell RNA-Seq

E12.5 murine *Nos3*$^{-/-}$ (N=4) and wild type (N=4) embryos were collected in cold PBS after which the heart was dissected and the cardiac outflow tract was carefully isolated. Cardiac outflow tracts were incubated with 10% trypsin for 7 min at 37°C and resuspended on ice to obtain a single cell suspension. Cells were washed twice with PBS supplemented with 10% of fetal calf serum and transferred over a cell strainer prior to FACS sorting. Dying cells were labelled using DAPI (1/1000) and excluded from further sorting. Single cells were captured using a FACSAria III cell sorter (BD Biosciences) and distributed over 384 well plates containing CEL-Seq2 primer solution and mineral oil as described previously (Muraro *et al.*, 2016). The 384 well plates were immediately frozen on dry ice and stored at −80°C.

CEL-Seq2 primers and ERCC Spike-in RNA (0.02 µL of 1: 50.000 dilution) were dispensed with the Mosquito HTS (TTPlabtech). Cell lysis was performed using heat shock incubation of cells for 5 minutes at 65°C. RT and second strand synthesis reagents were dispensed using the Nanodrop II (GC biotech) to generate barcoded cDNA libraries unique to each cell. The barcoded cDNA libraries in all wells were pooled prior to linear amplification in vitro. To generate Illumina sequencing libraries TruSeq small RNA primers (Illumina) were used for library PCR. Libraries were sequenced using 75 bp paired end sequencing using an Illumina Nextseq500 platform.

Paired end reads were mapped to the reference genome GRCm38/mm10 using the Burrows-Wheeler Aligner tool (version 0.7.17) (Li and Durbin, 2010).

The RaceID3 algorithm was used to cluster cells based on K-medoids clustering as described previously (Herman, Sagar and Grün, 2018). RaceID3 analysis was performed using an criteria of mintotal = 1000, excluding cells that had lower than 1000 unique transcripts. Further analysis used default parameters. Mitochondrial and ribosomal genes were excluded as the abundant expression interfered with downstream clustering. Cell clusters were visualized using t-distributed stochastic neighbor embedding (t-SNE) and differential expression of genes between subgroups of cells was calculated using the DESeq2 package in the R platform (Love, Huber and Anders, 2014; Grün *et al.*, 2015).

The R-code and documentation of RaceID3 is available for download at https://github.com/dgrun/RaceID3_StemID2_package (Herman, Sagar and Grün, 2018).

2.9 RNA isolation and quantitative real-time PCR (Q-PCR)

P6 month adult mice were euthanized using cervical dislocation after which the heart and aortic arch were isolated. Aortic samples were carefully dissected from the ascending aorta minimizing any external tissue contamination. Whole tissue RNA isolation of *Nos3*$^{-/-}$ (N=5, of which 2 females and 3 males) and wild type mice (N=5, of which 2 females and 3 males) was performed using TRIzol reagent (Invitrogen) RNA isolation and gDNA removal using the TURBO DNA-Free kit (Invitrogen) followed by reverse transcription to obtain cDNA using Iscript cDNA synthesis kit (Bio-rad) according to manufacturer's protocols.

Quantitative PCR was performed with SYBR Green (Bio-rad) on the CFX384 Touch Real-Time PCR Detection System (Bio-rad). The PCR program ran a single cycle of 50°C (10 minutes) and by 95°C (5 minutes) followed by 40 cycles of 95°C (10 seconds) and 60°C (1 minute). Primers used in qPCR are described in table S1. qPCR was performed in triplicates and average Ct score was quantified relative to housekeeping gene *Rpl32* and *Gapdh*. Differential gene expression in ascending aortas of wild type and *Nos3*$^{-/-}$ mice was presented using Log2 fold change.

2.10. Statistical analysis

Results are represented as mean ± SD of at least three independent experiments. Statistical analyses were performed using unpaired two tailed Student's *t*-test. Significance was assumed when $p < 0.05$. Statistical analysis was performed in GraphPad Prism 8.0 for Windows (GraphPad Software, La Jolla California USA).

3. Results

3.1 Observation of aortic dissection in Nos3$^{-/-}$ mice.

The aortic vessel wall is primarily composed of radial sheets of elastin in between layers of VSMCs in the tunica media (Fig. 1). Extracellular collagen contributes mostly to the fibrous structures found in the adventitia of the aortic vessel wall (Fig. S1). Histological examination of aortic vessel walls in *Nos3*$^{-/-}$ mice revealed morphological signatures of spontaneous aortic dissections as a result of local disruptions within the aortic vessel wall (Fig. 1,Fig. S1). The aortic dissection was located slightly above the sinotubular junction in *Nos3*$^{-/-}$ mice. Adventitial tissue remodelling low in elastin and collagen content in response to aortic dissection was observed in the dissected aortic vessel wall of *Nos3*$^{-/-}$ mice (Fig. 1G,Fig. S1).

The spontaneous development of aortic dissections seen in *Nos3*$^{-/-}$ mice have been sparsely distributed within the dataset occurring in ~13% of *Nos3*$^{-/-}$ mice (4/31 *Nos3*$^{-/-}$ mice) ranging in stages from 1 month to 11 months of age. Dissection occurred in both BAV (N=1) (Fig. S1) and TAV (N=3) *Nos3*$^{-/-}$ mice. Survival analysis indicated no difference in the temporal distribution of spontaneous death events between wild type and *Nos3*$^{-/-}$ populations (Fig. S2).

3.2 Nos3$^{-/-}$ mice develop aortic dilation early into adulthood.

To examine whether the aortic dissections coincide with an increased aortic diameter, ultrasound imaging was used to visualize the aorta of wild type and *Nos3*$^{-/-}$ mice *in vivo* (Fig. 2A-D). Careful measurements of the proximal-, mid-, and distal-ascending aorta were made to determine aortic diameters during systole and diastole (Fig. 2E-F). Aortic ultrasound measurements in 4 month-old adult mice showed no difference in aortic diameter during peak systole (Fig. 2E). However, peak diastolic aortic measurements determined significant larger aortic diameters in the prox- and distal-ascending aorta of *Nos3*$^{-/-}$ mice (Fig. 2F).

Moreover, aortic strain calculations determined significant reductions in circumferential strain in the prox-ascending aorta of *Nos3*$^{-/-}$ mice (Fig. 2G).

3.3 Reduced elastic fibres in ascending aortic vessel walls of Nos3$^{-/-}$*mice.*

The morphologic structure of the ECM within the ascending aorta was analysed at adult as well as embryonic (E17.5) stages of development to examine onset of vascular wall pathology (Fig. 3). Volumetric quantification of elastic lamellae within the vessel wall of the ascending aorta showed significant reductions in the volume of elastic fibres within vessel walls of *Nos3*$^{-/-}$ mice at embryonic as well as adult stages. Morphological comparison of the elastic lamellae in aortic vessel walls indicated that disruptions in elastic fibres impacted the inner medial region of the aortic vessel wall. The aortic vessel wall of wild type mice consisted of an inner media of densely packed sinuous elastic lamella and an outer media of smoothly aligned elastin lamellae (Fig. 3A). In contrast, the aortic vessel wall of adult *Nos3*$^{-/-}$ mice solely developed smoothly aligned elastin lamellae throughout the complete aortic vessel wall (Fig. 3B).

In addition to elastin, collagen disposition was also examined in aortic vessel walls of adult and embryonic mice (Fig. S3). Volumetric collagen analysis of medial and adventitial aortic collagen deposition determined no significant indicating that the *Nos3* mutation does not impact collagen deposition within ascending aortic walls of embryonic or adult mice but specifically affects formation of elastic lamellae in the aortic vessel wall (Fig. S3E-H).

3.4 NCC populations are reduced in aortic vessel walls of Nos3$^{-/-}$ *embryos.*

The observation of elastin disruption within the inner media suggested a possible role of the NCC lineage in aortopathy. Previous findings from our lab already established NCC lineage disruption in aortic valves during cushion development in *Nos3*$^{-/-}$ embryos (Peterson *et al.*, 2018). Genetic lineage tracing using *Wnt1Cre;mTmG* and *Nos3*$^{-/-}$*;Wnt1Cre;mTmG* embryos (E17.5 and E12.5) showed NCC-derived VMSCs line the entire inner media of the ascending aorta (Fig. 4, Fig. S4). Comparison of the NCC-derived cell populations in the ascending aortic vessel wall between wild type and *Nos3*$^{-/-}$ embryos showed a significant reduction of NCCs in the aortic vessel wall of *Nos3*$^{-/-}$ embryos at both E17.5 and E12.5 (Fig. 4C,F). Close morphological examination revealed incomplete coverage in the inner media of the ascending aorta by NCCs-derived cells in *Nos3*$^{-/-}$ embryos. Three-dimensional reconstruction of the E12.5 outflow tract indicates the reduction in NCCs derived cells to be limited to the ascending aorta (Fig. 4G,H).

3.5 Single cell RNA sequencing reveals downregulation of genes associated with aortopathy in VSMCs of Nos3$^{-/-}$ mice.

To investigate the effects of the *Nos3* mutation on a transcriptional level, single cell RNA-seq was used on the murine outflow tract of E12.5 embryos. K-medoids clustering using the Race-ID3 algorithm (Herman, Sagar and Grün, 2018) defined 16 cell clusters based on similarities in cellular gene expression in the outflow tract of wild type origin (Fig. 5). Individual clusters were examined for known marker genes to identify cell types corresponding to each cluster. Using this approach we identified multiple cell types namely, VSMCs, cushion mesenchyme, cardiomyocytes, and leukocytes.

Combined clustering of wild type and *Nos3*$^{-/-}$ single cell transcriptomes allowed for an unbiased assessment of cell type differences as clustering depends on cellular likeliness based on gene expression. Two clusters were found in close proximity of each other, in which wild type (cluster 1) and *Nos3*$^{-/-}$ (cluster 15) derived cells formed separate near homogenous groups (Fig. 6A-D).

Based on the relative high *Acta2* and *Tagln* RNA expression levels within the clusters these were identified as VSMCs. Differential gene expression analysis between wild type and *Nos3*$^{-/-}$ VSMC clusters revealed significant differences in gene expression of a total of 45 genes (30 upregulated and 15 downregulated genes) of which the top upregulated gene was *Acta2*, and top downregulated gene was *Eln* in *Nos3*$^{-/-}$ VSMCs. (Fig. 6E-F, Fig. S5). This study focused on downregulated genes as BAV and BAV-related aortopathy are often associated with gene mutations resulting in downregulated gene expression (Prakash *et al.*, 2014). The absence of *Nos3* induced NO signalling resulted most notably in the down regulation of *Eln* transcription, a gene encoding for elastin a major component of elastic fibres (Fig. 6E,G). VSMCs of *Nos3*$^{-/-}$ also had decreased expression of *Fbln5*, which translates to fibulin-5, another important protein which directly interacts with elastin for the formation of elastic fibres in the ECM (Midwood and Schwarzbauer, 2002; Yanagisawa *et al.*, 2002). Interestingly, multiple genes, *Eln, Fbln5, Cxcl12, Fn1, Gata6, Mfap4* were found to be downregulated in *Nos3*$^{-/-}$ VSMCs; genes which are all associated with BAV and aneurysm formation (Midwood and Schwarzbauer, 2002; Ogata *et al.*, 2005; Paloschi, Kurtovic, Folkersen, Gomez, Wågsäter, *et al.*, 2011; Orriols *et al.*, 2016; Girdauskas *et al.*, 2017; Zhang *et al.*, 2018) (Fig. 6G). To ascertain that the changes in gene expression were not limited to stages of embryonic development, qPCR was performed for the top 3 differential expressed genes on ascending aortic tissues from adult wild type and *Nos3*$^{-/-}$ mice. qPCR analysis determined similar upregulation of *Acta2* and downregulation of *Eln* and *Fbln5*

expression as seen in the RNA-seq analysis of E12.5 embryos indicating that these findings persist into adulthood (Fig. 6H, Fig. S6).

3.6 Genetic misregulation translates into altered protein expression phenotypes and is most pronounced in NCC-derived VSMCs of Nos3$^{-/-}$ mice.

To examine the effects of aberrant RNA expression profiles found in the VSMCs of *Nos3*$^{-/-}$ embryos immunofluorescent antibody stainings were performed to examine localized alterations in protein translation within the aortic vessel wall of E17.5 embryos (Fig. 7). Interestingly, FBLN5 expression was most pronounced in NCC-derived VSMCs of wild type embryos (Fig. 7A,C). On the contrary, NCC-derived VSMCs *Nos3*$^{-/-}$ did not accumulate FBLN5 in accordance to a phenotype of reduced *Fbln5* expression (Fig. 7B,D). Moreover, ACTA2 expression was also more pronounced in NCC-derived VSMCs in both wild type and *Nos3*$^{-/-}$ embryos than VSMCs from a different origin (Fig. 7E-H, Fig. S4). Nonetheless, the differences in ACTA2 expression between wild type and *Nos3*$^{-/-}$ embryos would support a phenotype of *Acta2* overexpression within the NCC-derived VSMCs of *Nos3*$^{-/-}$ embryos.

The protein expression dynamics of both FBLN5 and ACTA2 were in agreement to the findings of those predicted by scRNA-seq and qPCR. These findings demonstrate the importance of NO-signalling for maintaining the vessel wall integrity of the ascending aorta.

Discussion

Patients with a BAV have a higher risk to develop aortopathy of the ascending aorta. The exact mechanisms through which BAV-associated aortopathy arises are still poorly understood. Knowledge of the underlying processes could advance patient risk assessments and aid in the development of early diagnostic tools.

We examined the impact of NO depletion to identify effects of BAV-associated aortopathy in mice. We describe for the first time that *Nos3*$^{-/-}$ mice develop dissections in the ascending aorta by affecting signalling pathways involved in elastic fibre formation.

Studies by Koenig and colleagues, have reported evidence of aortopathy in mice with haploinsufficiency of *Notch1* in a *Nos3*$^{-/-}$ mixed background (Koenig *et al.*, 2015). Later studies of the same group, however, reported *Notch1* haploinsufficiency in 129SV mice also caused ascending aortic aneurysm making the role of *Nos3* in aortopathy less clear (Koenig *et al.*, 2017). Reports examining HPH-1 mice, a mouse model with uncoupled NOS3, showed rapidly developing abdominal aortic aneurysms as well as aortic rupture upon

infusion of ANGII (Gao *et al.*, 2012). Moreover, Fan and colleagues showed that ANGII infusion could also lead to abdominal aortic dissection through endothelial mediated reactive oxygen signalling in wild type mice (Fan *et al.*, 2014). Reports by Kuhlencordt and colleagues show that double knockout *apoE/Nos3* models develop severe cardiovascular complications including spontaneous abdominal aortic aneurysms and dissection (Kuhlencordt *et al.*, 2001). These studies all suggest *Nos3* to be an important gatekeeper of the aortic vessel wall which acts in combination with other factors to maintain aortic stability, yet is unable to result in aortopathy in case singular gene function is lost.

The spontaneous aortic dissections found in *Nos3*$^{-/-}$ mice in this study might have been overlooked by previous studies as the age of onset from this study was distributed over a period of 11 months. *Nos3*$^{-/-}$ mice in which dissections were found were acquired during routine investigations. Hemorrhages found within dissected mice were limited to the subepicardial space and were not found within the pericardial cavity or the mediastinum. This could suggest that these mice were collected during a window in which the mice were still viable but at high risk to succumb by further aortic deterioration. The mortality rate in humans is known to increase to 70% within 48h after aortic dissection (Hagan *et al.*, 2000; Criado, 2011) and *Nos3*$^{-/-}$ mice might face an equal rapid increase of mortality rate after the onset of aortic dissection, nevertheless, the observation of aortic remodelling in *Nos3*$^{-/-}$ mice might challenge this concept. The survival analysis did not reveal a specific interval at which *Nos3*$^{-/-}$ mice spontaneous deaths differed from wild type populations, complicating the acquisition of mice prone to dissect. Future studies should look more specific into the mortality rate related to aortic dissection in *Nos3*$^{-/-}$ to better apprehend the timing and risks involved in the development of an aortic dissection.

Ultrasound measurements of the aorta showed increased aortic diameters in 4 months old *Nos3*$^{-/-}$ mice. These results suggest that the aortic vessel wall developed structural aortic dilations in adulthood similar to aortic aneurysm development observed in BAV patients (Cecconi *et al.*, 2006). Circumferential aortic strain, a measure of aortic elasticity, is known to decrease with age and has been explored in clinical studies to examine aortic stiffness and is considered an important cardiovascular risk factor for patient health (Redheuil *et al.*, 2010). Moreover, in Marfan mouse models circumferential aortic strain has been shown to correlate with elastin fragmentation and reduced elastic lamellae in aortic vessel walls (Mariko *et al.*, 2011; Chen *et al.*, 2019).

The aorta and the aortic valve have a similar developmental origin involving contributions of endothelial, NCC and second heart field lineages. BAV patients have increased risks to

develop aneurysms and dissections of the ascending aorta but not of the descending aorta (Biner *et al.*, 2009). NCCs are known to contribute to the formation of the VSMCs of the aortic root, ascending aorta, and aortic arch. The reduction in the NCC-derived populations was observed in the ascending aorta of E12.5 and E17.5 *Nos3*$^{-/-}$ embryos which was most notable in the region of the commissures. NCCs have been reported to accumulate in the commissures, however their function there is still poorly understood (Badger *et al.*, 2010; Orriols *et al.*, 2016). Previous studies have shown the importance of correct NCC distribution for proper aortic valve and outflow tract formation (Paloschi, Kurtovic, Folkersen, Gomez, Wagsater, *et al.*, 2011; Peterson *et al.*, 2018; Zhang *et al.*, 2018). Moreover, BAV patients and their first degree relatives have increased risk aortopathy, suggesting that the underlying mechanisms are not limited solely to BAV cases (Biner *et al.*, 2009). Our findings were derived from *Nos3*$^{-/-}$ which were not selected *a priori* for BAV or TAV phenotype but *Nos3*$^{-/-}$ mice have been known to develop BAV in ~25% of the cases (Fernandez *et al.*, 2009; Peterson *et al.*, 2018). This study found aortic dissection in both TAV and BAV *Nos3*$^{-/-}$ mice similar to patient observations suggesting a role for NO signalling in aortic development in both human and mice.

This study found the significant downregulation of elastin in VSMCs in both protein and RNA expression to result in aortic dissection in *Nos3*$^{-/-}$ mice. Interestingly, clinical studies show that the elastin content is generally decreased in the ascending aortic wall of dissected patients when compared to controls (Cattell, Hasleton and Anderson, 1993). Decreased elastin concentrations within the aortic wall is strongly correlated with decreased expression of *Fbln5* in patients with ascending aortic dissection similar to results found in *Nos3*$^{-/-}$ mice (Wang *et al.*, 2005). Whilst elastic fibre degeneration in dissected aortic patients is often attributed to increased activity of metalloproteases (MMPs) (Zhang, Shen and LeMaire, 2011), *Nos3*$^{-/-}$ mice have decreased NO production inhibiting MMP activity (Ridnour *et al.*, 2007). Elastic fibre degeneration might also be the result of reduced *Fbln5* expression as FBLN5 can function as scaffolding protein during elastic fibre assembly (Midwood and Schwarzbauer, 2002). *Fbln5*$^{-/-}$ mice show reduced contractility in the thoracic aorta (Murtada *et al.*, 2016) and develop hypertension (Le *et al.*, 2014) but do not give rise to aortic aneurysms or aortic dissection. Similarly, *Eln*$^{+/-}$ mice also show reduced aortic contractility and increasing blood pressure (Jiang *et al.*, 2000; Jain *et al.*, 2011). In humans, hypertension is the single most important risk factor for aortic dissection (Hagan *et al.*, 2000). Interestingly *Nos3*$^{-/-}$ mice have been described to also exhibit high blood pressure (Huang *et al.*, 1995). The exact mechanisms how *Nos3* would give rise to aortic dilation and dissection is not yet fully understood. Given that NCC populations were found reduced within the inner media of *Nos3*$^{-/-}$ embryos this might suggest a novel role of NO signalling during

development. Genetic predisposition of aortic root aneurysm pathogenesis has been observed as a result of lineage-specific events related to NCC derived VSMCs in Loeys-Dietz syndrome, a disease in which BAVs are more frequently observed than in the general population (MacCarrick *et al.*, 2014; MacFarlane *et al.*, 2019). This study also found most changes related to gene expression within the aortic vessel wall to be most prominent in NCC derived VSMCs of *Nos3*$^{-/-}$ mice. The NCC derived VSMCs populate the inner media of the aorta and might depend on the paracrine cues of NO signalling for proper functioning. Interestingly, Kong and colleagues show that inhibition of NO signalling during development affected cranial neural crest patterning, differentiation and convergence in the pharyngeal arch, demonstrating a coordinating role of NO signalling during development (Kong *et al.*, 2014). Moreover, Suvorava and colleagues show that *Nos3*$^{-/-}$ rescue through additional NO supplementation did not result in reduced hypertension in 3-4 month adult *Nos3*$^{-/-}$ mice supporting an extra-endothelial role of *Nos3* (Suvorava *et al.*, 2015). Effects of NO signalling on cellular function are diverse as NO is known to act on multiple kinase signalling cascades (Schindler and Bogdan, 2001) and affect multiple transcription factors through NF-kB, c-Fos/Jun, Sp1, Egr-1, VDR/RXR and HIF-1 interaction (Bogdan, 2001; Hemish *et al.*, 2003). This makes it challenging to interpret primary pathways involved during outflow tract formation. Future studies focusing on the molecular interactions between endothelial cells and NCC during development should provide more insight into the signalling routes through which *Nos3* acts during development.

The role of *Nos3* in thoracic aneurysms, aortic dissections and BAV in humans is still poorly understood. In multiple human studies disruptions of *Nos3* signalling in ascending aortic walls of BAV patients (Ridnour *et al.*, 2007; Zhang, Shen and LeMaire, 2011). Moreover, a small patient study reported that polymorphisms in *Nos3* were associated with aortic dissections in patients with thoracic aortic aneurysms (Ekmekçį *et al.*, 2014). These reports suggest that disrupted NO signalling impacts pathologic onset in the human thoracic aorta. Nevertheless, more recently a large cohort study reported no significant associations between *Nos3* and BAV patients with thoracic aneurysms suggesting that *Nos3* polymorphisms might be even protective for of aneurysm development in BAV patients (Gillis *et al.*, 2017). Although the exact role of *Nos3* in thoracic aneurysm, aortic dissection and its relation to BAV is not yet fully understood in humans, these reports support an important role of *Nos3* in maintaining vessel wall integrity.

Conclusion

This study examined the developmental processes involved in aortic aneurysm formation and found dissections in ~13% of *Nos3*$^{-/-}$ mice aged from 1 to 11 months, of which 25% had a BAV. Ultrasound imaging showed that *Nos3*$^{-/-}$ mice develop aortic dilations into adulthood similar to observations in BAV patients. The dissections were a result of disruption in elastin by VSMCs. A reduction in NCC-derived VSMCs which populate the inner aortic media was observed during mid gestation and late embryonic development of *Nos3*$^{-/-}$ mice, supporting a congenital predisposition for developing BAV-associated aortopathy. Single cell sequencing of embryonic outflow tracts showed significant downregulation of *Eln* and *Fbln5* mRNA in VSMCs of *Nos3*$^{-/-}$ mice which was also confirmed in ascending aortic tissue of adult mice showing that the embryonic disruptions in elastic lamellae formation persisted into adulthood. Downregulation of *Eln* and *Fbln5* translated into reduced ELN and FBLN5 protein translation which primarily affected NCC-derived VSMCs. Disrupted endothelial mediated NO signalling causes congenital BAV-associated aortic dilation and dissection as a result of inhibited elastic lamellae formation in VSMCs in *Nos3*$^{-/-}$ mice.

Acknowledgements

None

Competing interests

No competing interests declared

Funding

Funding and salary support were provided by The Dutch Heart foundation (Project code: 31190BAV).

References

Badger, S. A. *et al.* (2010) 'Common polymorphisms of Fibulin-5 and the risk of abdominal aortic aneurysm development', *Vascular Medicine*, 15(2), pp. 113–7. doi: 10.1177/1358863X09355667.

Biner, S. *et al.* (2009) 'Aortopathy Is Prevalent in Relatives of Bicuspid Aortic Valve Patients', *Journal of the American College of Cardiology*, 53(24), pp. 2288–2295. doi: 10.1016/j.jacc.2009.03.027.

Bogdan, C. (2001) 'Nitric oxide and the regulation of gene expression', *Trends in Cell Biology*, 11(2), pp. 66–75. doi: 10.1016/S0962-8924(00)01900-0.

Cardiff, R. D., Miller, C. H. and Munn, R. J. (2014) *Manual hematoxylin and eosin staining of mouse tissue sections*, *Cold Spring Harbor Protocols*. doi: 10.1101/pdb.prot073411.

Cattell, M. A., Hasleton, P. S. and Anderson, J. C. (1993) 'Increased elastin content and decreased elastin concentration may be predisposing factors in dissecting aneurysms of human thoracic aorta', *Cardiovascular Research*, 27(2), pp. 176–81. doi: 10.1093/cvr/27.2.176.

Cecconi, M. *et al.* (2006) 'Aortic dilatation in patients with bicuspid aortic valve', *J Cardiovasc Med (Hagerstown)*, 7(1), pp. 11–20. doi: 10.2459/01.JCM.0000199777.85343.ec.

Chen, J. Z. *et al.* (2019) 'Aortic Strain Correlates With Elastin Fragmentation in Fibrillin-1 Hypomorphic Mice', *Circulation Reports*. doi: 10.1253/circrep.cr-18-0012.

Criado, F. J. (2011) 'Aortic dissection: a 250-year perspective.', *Texas Heart Institute journal*, 38(6), pp. 694–700.

Culling, C. F. A. (1974) *Handbook of Histopathological and Histochemical Techniques*. 3rd edn, *Handbook of Histopathological and Histochemical Techniques*. 3rd edn. doi: 10.1016/c2013-0-04011-x.

Ekmekcį, A. *et al.* (2014) 'Association between endothelial nitric oxide synthase intron 4a/b polymorphism and aortic dissection', *Turk Kardiyoloji Dernegi Arsivi*, 42(1), pp. 55–60. doi: 10.5543/tkda.2014.88269.

Fan, L. M. *et al.* (2014) 'Endothelial cell-specific reactive oxygen species production increases susceptibility to aortic dissection', *Circulation*, 129(25), pp. 2661–72. doi: 10.1161/CIRCULATIONAHA.113.005062.

Fernandez, B. *et al.* (2009) 'Bicuspid aortic valves with different spatial orientations of the leaflets are distinct etiological entities', *J Am Coll Cardiol*, 54(24), pp. 2312–2318. doi: 10.1016/j.jacc.2009.07.044.

de Figueiredo Borges, L. *et al.* (2008) 'Collagen is reduced and disrupted in human aneurysms and dissections of ascending aorta', *Human Pathology*, 39(3), pp. 437–43. doi: 10.1016/j.humpath.2007.08.003.

Gao, L. *et al.* (2012) 'Role of uncoupled endothelial nitric oxide synthase in abdominal aortic aneurysm formation: Treatment with folic acid', *Hypertension*, 59(1), pp. 158–66. doi: 10.1161/HYPERTENSIONAHA.111.181644.

Gharibeh, L. *et al.* (2018) 'GATA6 regulates aortic valve remodeling, and its haploinsuffciency leads to right-left type bicuspid aortic valve', *Circulation*, 138(10), pp. 1025–1038. doi: 10.1161/CIRCULATIONAHA.117.029506.

Gillis, E. *et al.* (2017) 'Candidate gene resequencing in a large bicuspid aortic valve-associated thoracic aortic aneurysm cohort: SMAD6 as an important contributor', *Frontiers in Physiology*, 13(8), p. 400. doi: 10.3389/fphys.2017.00400.

Girdauskas, E. *et al.* (2017) 'Genetic abnormalities in bicuspid aortic valve root phenotype: preliminary resultsdagger', *Eur J Cardiothorac Surg*, 52(1), pp. 156–162. doi: 10.1093/ejcts/ezx065.

Goergen, C. J. *et al.* (2010) 'In vivo quantification of murine aortic cyclic strain, motion, and curvature: implications for abdominal aortic aneurysm growth.', *Journal of magnetic resonance imaging : JMRI*, 32(4), pp. 847–58. doi: 10.1002/jmri.22331.

Grün, D. *et al.* (2015) 'Design and Analysis of Single-Cell Sequencing Experiments', *Cell*, 163(4), pp. 799–810. doi: 10.1016/j.cell.2015.10.039.

Hagan, P. G. *et al.* (2000) 'The International Registry of Acute Aortic Dissection (IRAD): New insights into an old disease', *Journal of the American Medical Association*, 283(7), pp. 897–903. doi: 10.1001/jama.283.7.897.

Hemish, J. *et al.* (2003) 'Nitric Oxide Activates Diverse Signaling Pathways to Regulate Gene Expression', *Journal of Biological Chemistry*, 278(43), pp. 42321–9. doi: 10.1074/jbc.M308192200.

Herman, J. S., Sagar and Grün, D. (2018) 'FateID infers cell fate bias in multipotent progenitors from single-cell RNA-seq data', *Nature Methods*, 15(5), pp. 379–386. doi: 10.1038/nmeth.4662.

Huang, P. L. *et al.* (1995) 'Hypertension in mice lacking the gene for endothelial nitric oxide synthase', *Nature*, 377(6546), pp. 239–42. doi: 10.1038/377239a0.

Isselbacher, E. M. (2005) 'Thoracic and Abdominal Aortic Aneurysms', *Circulation*, 111(6), pp. 816–828. doi: 10.1161/01.CIR.0000154569.08857.7A.

Jain, R. *et al.* (2011) 'Cardiac neural crest orchestrates remodeling and functional maturation of mouse semilunar valves', *Journal of Clinical Investigation*, 121(1), pp. 422–430. doi: 10.1172/JCI44244.

Jiang, X. *et al.* (2000) 'Fate of the mammalian cardiac neural crest', *Development*, 127(8), pp. 1607–1616.

Junqueira, L. C. U., Bignolas, G. and Brentani, R. R. (1979) 'A simple and sensitive method for the quantitative estimation of collagen', *Analytical Biochemistry*. doi: 10.1016/0003-2697(79)90795-4.

Koenig, S. *et al.* (2015) 'Evidence of Aortopathy in Mice with Haploinsufficiency of Notch1 in Nos3-Null Background', *Journal of Cardiovascular Development and Disease*, 2(1), pp. 17–30. doi: 10.3390/jcdd2010017.

Koenig, S. N. *et al.* (2017) 'Notch1 haploinsufficiency causes ascending aortic aneurysms in mice', *JCI Insight*, 2(21). doi: 10.1172/jci.insight.91353.

Kong, Y. *et al.* (2014) 'Neural crest development and craniofacial morphogenesis is coordinated by nitric oxide and histone acetylation', *Chemistry and Biology*, 21(4), pp. 488–501. doi: 10.1016/j.chembiol.2014.02.013.

Kuhlencordt, P. J. *et al.* (2001) 'Accelerated atherosclerosis, aortic aneurysm formation, and ischemic heart disease in apolipoprotein E/endothelial nitric oxide synthase double-knockout mice', *Circulation*, 104(4), pp. 448–454. doi: 10.1161/hc2901.091399.

Laforest, B., Andelfinger, G. and Nemer, M. (2011) 'Loss of Gata5 in mice leads to bicuspid aortic valve', *Journal of Clinical Investigation*, 121(7), pp. 2876–2887. doi: 10.1172/JCI44555.

Le, V. P. *et al.* (2014) 'Fibulin-5 null mice with decreased arterial compliance maintain normal systolic left ventricular function, but not diastolic function during maturation', *Physiological Reports*, 2(3), p. E00257. doi: 10.1002/phy2.257.

Lee, T. C. *et al.* (2000) 'Abnormal aortic valve development in mice lacking endothelial nitric oxide synthase', *Circulation*, 101(20), pp. 2345–2348. doi: 10.1161/01.CIR.101.20.2345.

Li, H. and Durbin, R. (2010) 'Fast and accurate long-read alignment with Burrows-Wheeler transform', *Bioinformatics*, 26(5), pp. 589–95. doi: 10.1093/bioinformatics/btp698.

Loscalzo, M. L. *et al.* (2007) 'Familial thoracic aortic dilation and bicommissural aortic valve: A prospective analysis of natural history and inheritance', *American Journal of Medical Genetics, Part A*. doi: 10.1002/ajmg.a.31872.

Love, M. I., Huber, W. and Anders, S. (2014) 'Moderated estimation of fold change and dispersion for RNA-seq data with DESeq2.', *Genome biology*, 15(12), p. 550. doi: 10.1186/s13059-014-0550-8.

MacCarrick, G. *et al.* (2014) 'Loeys-Dietz syndrome: A primer for diagnosis and management', *Genetics in Medicine*. doi: 10.1038/gim.2014.11.

MacFarlane, E. G. *et al.* (2019) 'Lineage-specific events underlie aortic root aneurysm pathogenesis in Loeys-Dietz syndrome', *Journal of Clinical Investigation*. doi: 10.1172/JCI123547.

Mariko, B. *et al.* (2011) 'Fibrillin-1 genetic deficiency leads to pathological ageing of arteries in mice', *Journal of Pathology*, 224(1), pp. 33–44. doi: 10.1002/path.2840.

Midwood, K. S. and Schwarzbauer, J. E. (2002) 'Elastic fibers: Building bridges between cells and their matrix', *Current Biology*, 12(8), pp. R279-81. doi: 10.1016/S0960-9822(02)00800-X.

Muraro, M. J. *et al.* (2016) 'A Single-Cell Transcriptome Atlas of the Human Pancreas', *Cell Systems*, 3(4), pp. 385–394. doi: 10.1016/j.cels.2016.09.002.

Murtada, S.-I. *et al.* (2016) 'Reduced Biaxial Contractility in the Descending Thoracic Aorta of Fibulin-5 Deficient Mice', *Journal of Biomechanical Engineering*, 138(5), p. 051008. doi: 10.1115/1.4032938.

Ogata, T. *et al.* (2005) 'Genetic analysis of polymorphisms in biologically relevant candidate genes in patients with abdominal aortic aneurysms', *Journal of Vascular Surgery*, 41(6), pp. 1036–42. doi: 10.1016/j.jvs.2005.02.020.

Orriols, M. *et al.* (2016) 'Down-regulation of Fibulin-5 is associated with aortic dilation: Role of inflammation and epigenetics', *Cardiovascular Research*, 110(3), pp. 431–42. doi: 10.1093/cvr/cvw082.

Paloschi, V., Kurtovic, S., Folkersen, L., Gomez, D., Wågsäter, D., *et al.* (2011) 'Impaired splicing of fibronectin is associated with thoracic aortic aneurysm formation in patients with bicuspid aortic valve', *Arteriosclerosis, Thrombosis, and Vascular Biology*. doi:

Peterson, J. C. *et al.* (2018) 'Bicuspid aortic valve formation: Nos3 mutation leads to abnormal lineage patterning of neural crest cells and the second heart field', *Disease Models & Mechanisms*, 11(10), pp. 655–8. doi: 10.1242/dmm.034637.

Phillips, E. H. *et al.* (2018) 'Early pathological characterization of murine dissecting abdominal aortic aneurysms', *APL Bioengineering*, 2(4), p. 046106. doi: 10.1063/1.5053708.

Prakash, S. K. *et al.* (2014) 'A roadmap to investigate the genetic basis of bicuspid aortic valve and its complications: Insights from the international BAVCon (bicuspid aortic valve consortium)', *Journal of the American College of Cardiology*, 64(8), pp. 832–9. doi: 10.1016/j.jacc.2014.04.073.

Redheuil, A. *et al.* (2010) 'Reduced ascending aortic strain and distensibility: Earliest manifestations of vascular aging in humans', *Hypertension*, 55(2), pp. 319–26. doi: 10.1161/HYPERTENSIONAHA.109.141275.

Ridnour, L. A. *et al.* (2007) 'Nitric oxide regulates matrix metalloproteinase-9 activity by guanylyl-cyclase-dependent and -independent pathways', *Proceedings of the National Academy of Sciences*, 104(43), pp. 1689–16903. doi: 10.1073/pnas.0702761104.

Schindelin, J. *et al.* (2012) 'Fiji: An open source platform for biological image analysis.', *Nature Methods*, 9(7), pp. 676–682. doi: 10.1038/nmeth.2019.Fiji.

Schindler, H. and Bogdan, C. (2001) 'NO as a signaling molecule: effects on kinases', *International Immunopharmacology*, 1(8), pp. 1443–55. doi: 10.1016/s1567-5769(01)00089-3.

Suvorava, T. *et al.* (2015) 'Sustained hypertension despite endothelial-specific eNOS rescue in eNOS-deficient mice', *Biochemical and Biophysical Research Communications*, 458(3), pp. 576–583. doi: 10.1016/j.bbrc.2015.01.152.

Wang, X. *et al.* (2005) 'Decreased expression of fibulin-5 correlates with reduced elastin in thoracic aortic dissection', *Surgery*, 138(2), pp. 352–9. doi: 10.1016/j.surg.2005.06.006.

Yanagisawa, H. *et al.* (2002) 'Fibulin-5 is an elastin-binding protein essential for elastic fibre development in vivo', *Nature*, 415(6868), pp. 168–71. doi: 10.1038/415168a.

Zhang, J. *et al.* (2018) 'Significant Association of CXCL12 rs1746048 with LDL-C Level in Intracranial Aneurysms', *Current Neurovascular Research*, 15(1), pp. 26–33. doi: 10.2174/1567202615666180319153628.

Zhang, X., Shen, Y. H. and LeMaire, S. A. (2011) 'Thoracic Aortic Dissection: Are Matrix Metalloproteinases Involved?', *Vascular*, 17(3), pp. 147–157. doi: 10.2310/6670.2008.00087.

Figures

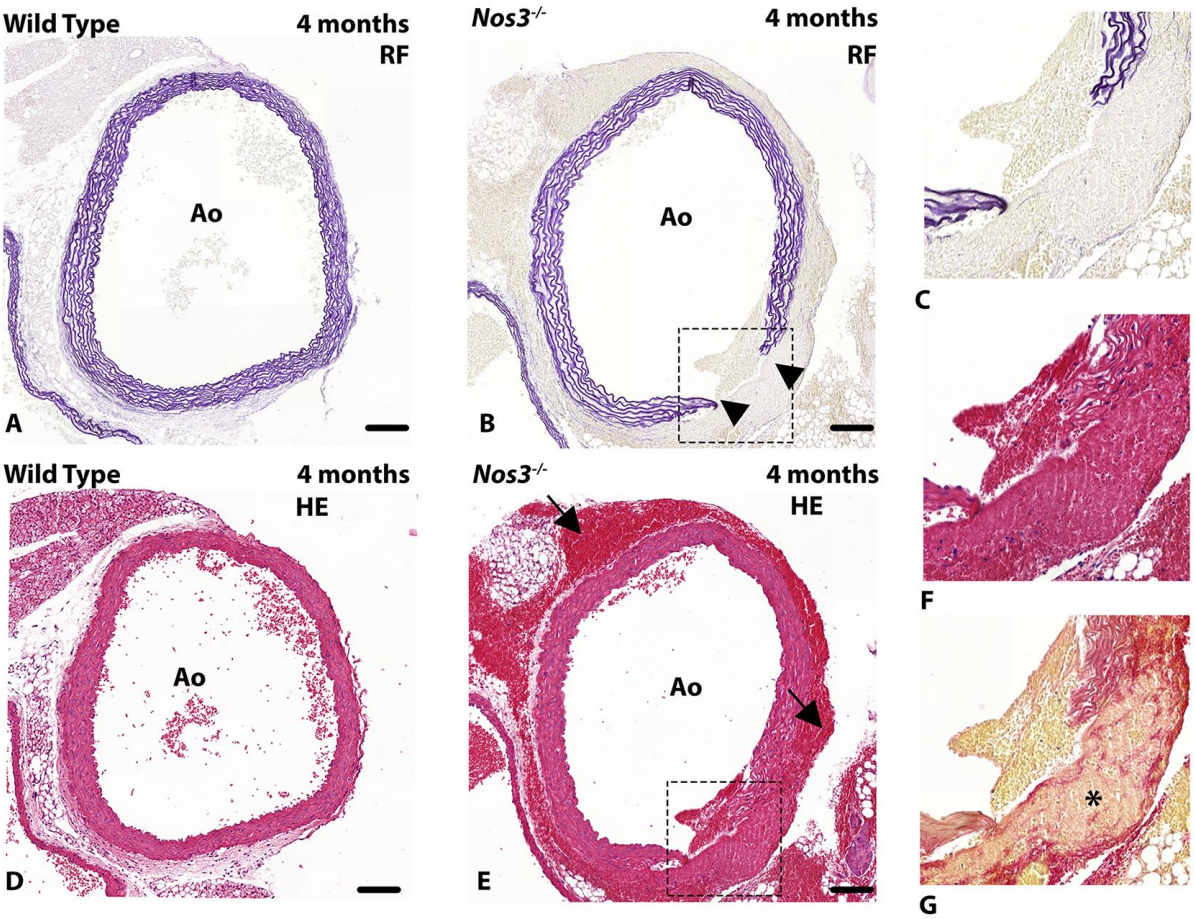

Figure 1. ***Aortic dissection in Nos3$^{-/-}$ mice.***

A-F: Transverse histological section of the ascending aorta in (A) wild type and (B-C) *Nos3*$^{-/-}$ mice stained with Resorcin-Fuchsin (RF) and Haematoxylin-Eosin (HE) (D-F). The *Nos3*$^{-/-}$ mice reveal rupture (arrow heads) of the elastic lamellae in the ascending aortic vessel wall located at or slightly above sinotubular junction. (G) Adjacent section stained for a combination collagen (red) and elastin (pink). Tissue remodelling of the adventitia can be observed in aortic vessel walls of dissected *Nos3*$^{-/-}$ mice (asterix). Blood deposits are present in the adventitia and subepicardial space (black arrows). Ao: Aorta. Scale bar: 100 µm

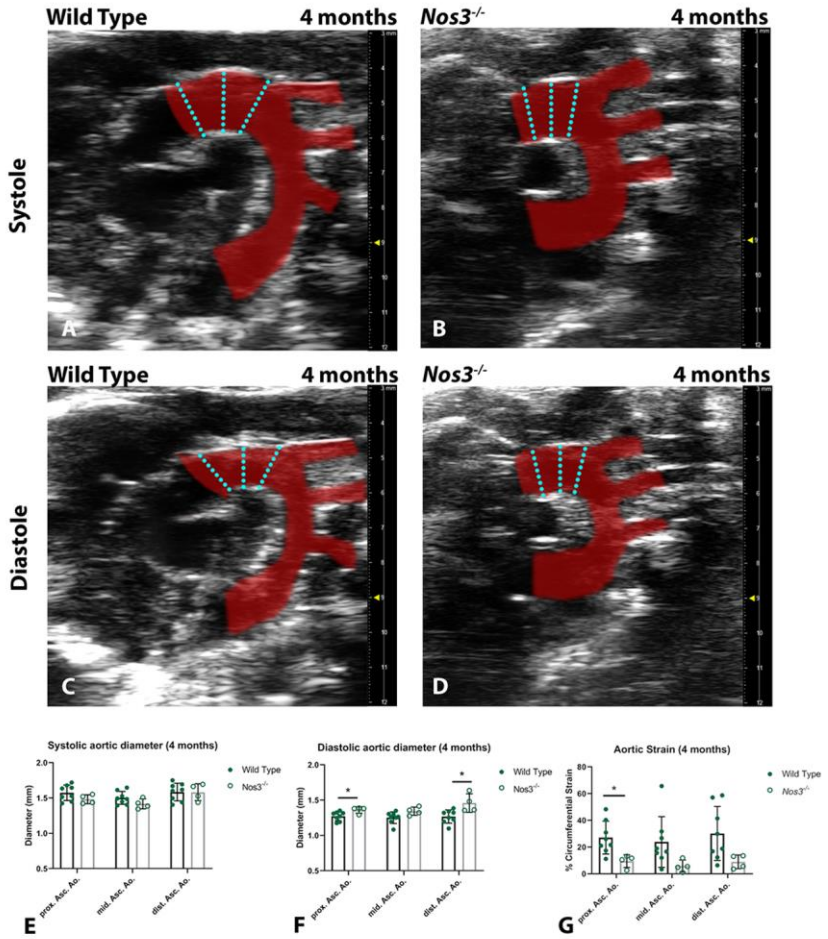

Figure 2. *Nos3*$^{-/-}$ mice develop aortic dilation at 4 months.

A-B: Ultrasound image of the aorta (red) during systole in (A) wild type and (B) *Nos3*$^{-/-}$ mice displays peak systolic diameter of the aorta. C-D: During diastole aortic diameter reaches maximum constriction in (C) wild type and (D) *Nos3*$^{-/-}$ mice. E-F: Aortic diameter were measured in wild type (N=8) and *Nos3*$^{-/-}$ (N=4) mice at the proximal-, mid-, and distal-ascending aorta (prox. Asc. Ao., mid. Asc. Ao., dist. Asc. Ao. respectively) in 4 months old mice at (E) peak systole and (F) peak diastole. Cyan dotted line indicate measurement locations of proximal, mid, and distal locations of the ascending aorta respectively. Two tailed student T-test showed *Nos3*$^{-/-}$ mice have significant larger diastolic diameters than wild type mice. G: Circumferential Green-Lagrange strain of the aorta was found significantly lower in the ascending aorta of *Nos3*$^{-/-}$ mice. *:P<0.05, **:P<0.01. Data are mean ± s.d.

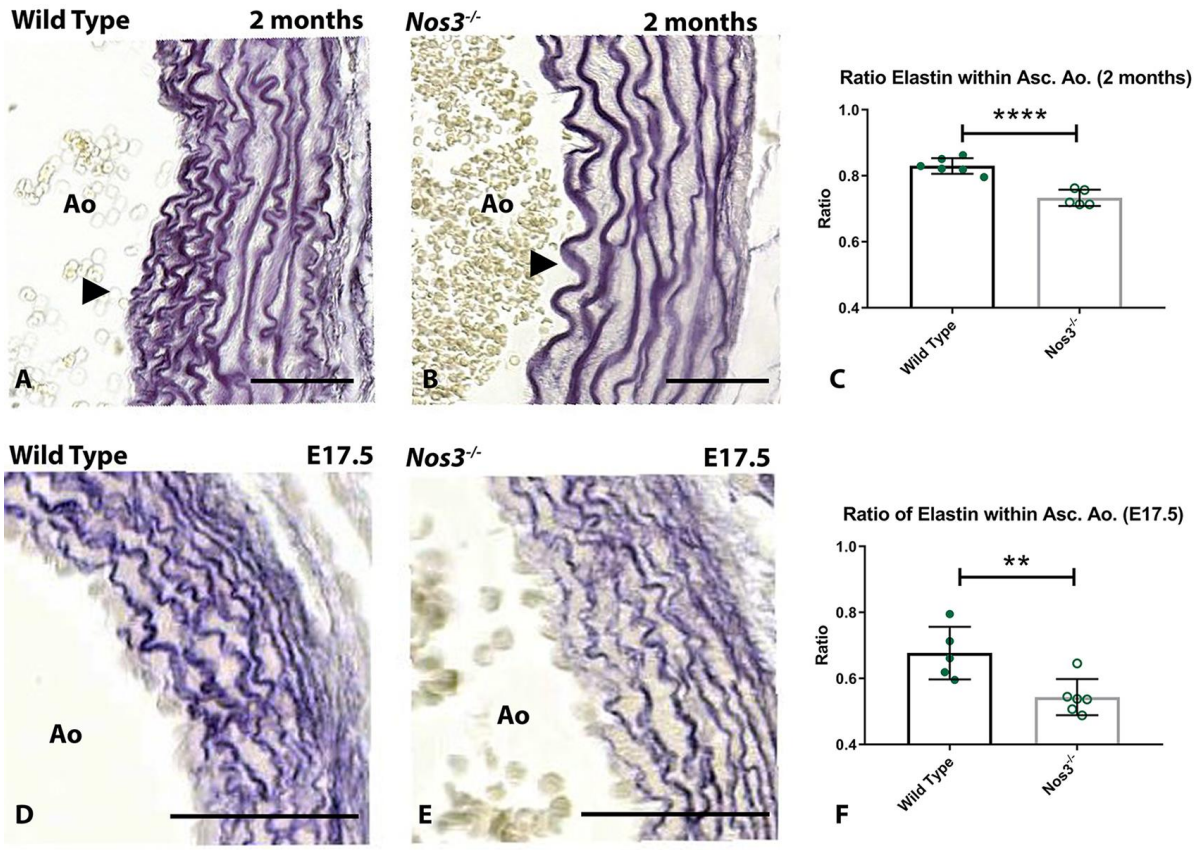

Figure 3. *Nos3*$^{-/-}$ aortic walls contain less elastin than wild type mice.

A-B: Transverse sections of aortic walls of adult (A) wild type and (B) *Nos3*$^{-/-}$ mice stained with resorcin-fuchsin to visualize elastin deposited as elastic fibres within the ascending aortic vessel wall. C: Volumetric quantification of elastin within the ascending aortic vessel wall of wild type (N=6) and *Nos3*$^{-/-}$ (N=5) adult (2 months) mice shows a reduction of elastin within aortic vessels of *Nos3*$^{-/-}$ mice. D-E: Resorcin-fuchsin staining of ascending aorta vessel walls of embryonic (E17.5) (D) wild type and (E) *Nos3*$^{-/-}$ mice. F: Volumetric quantification of elastic fibres in wild type (N=5) and *Nos3*$^{-/-}$ (N=6) embryos also shows significant reductions in volume of elastin within the ascending aorta in *Nos3*$^{-/-}$ embryos indicating impaired elastin production during embryogenesis. Morphological smooth elastin fibres, instead of densely packed sinuous lamella are observed within the inner media (arrowheads) of the aortic wall in *Nos3*$^{-/-}$ adult mice. Ao: Aorta, ****: P value <0.0001 **: P value <0.01 were determined by two tailed student T test. Scale bar: 50 µm. Data are mean ± s.d.

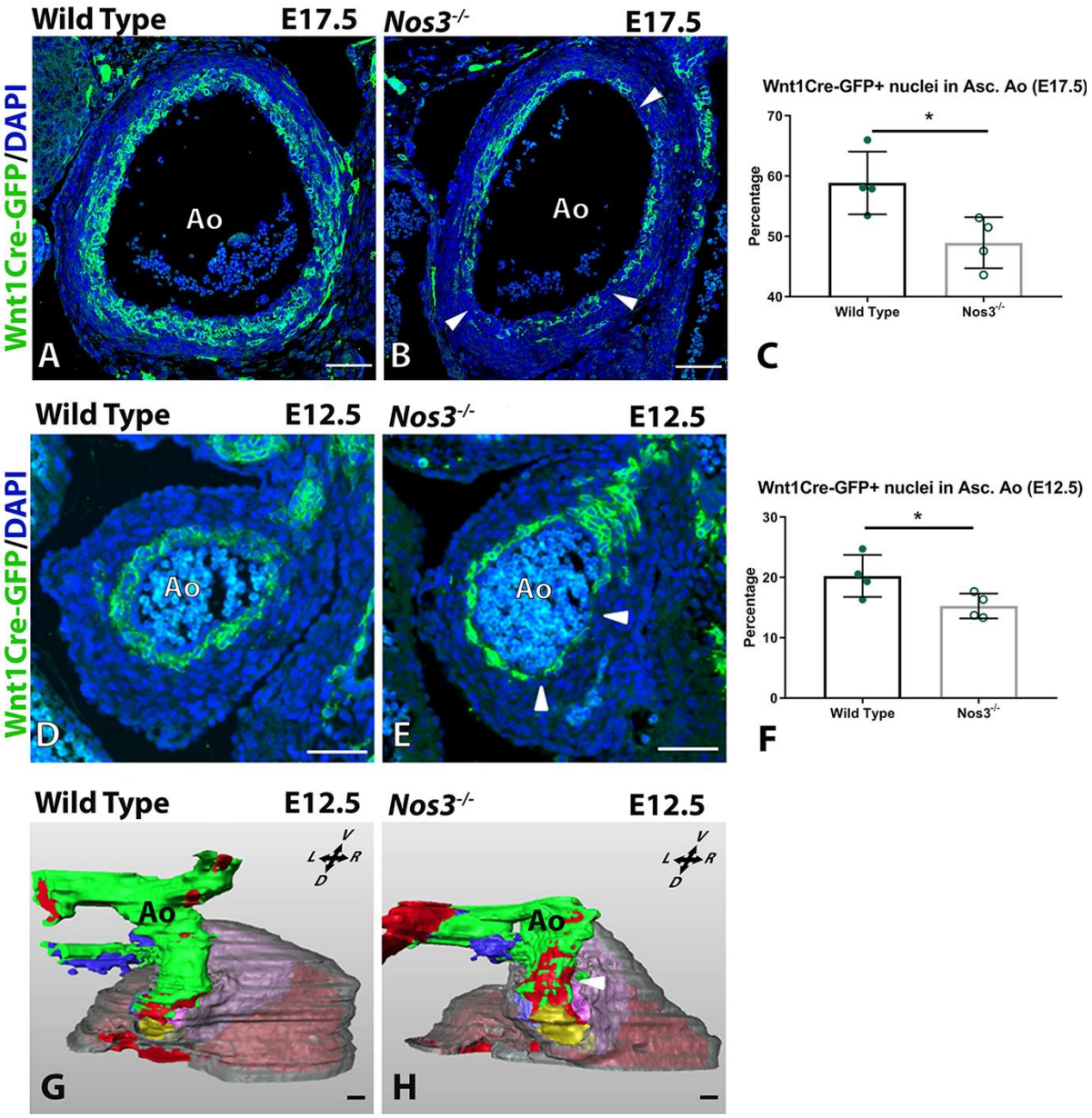

Figure 4. ***Reduction of the NCC population in aortic vessel walls of Nos3$^{-/-}$ embryos.***
A-B: Immunofluorescence staining of NCC-derived cells (green) in transverse sections of the ascending aortic vessel walls of (A) *Wnt1Cre^{+};mTmG* and (B) *Nos3$^{-/-}$;Wnt1Cre^{+};mTmG* embryos. C: Lineage quantification of NCC- derived cells showed a reduced contribution of NCC-derived cells in the vessel wall of the ascending aorta in *Nos3$^{-/-}$* (N=4) embryos when compared to wild type embryos (N=4) at E17.5. D-E: Immunofluorescent staining of NCC-derived cells in the ascending aortic vessel wall of E12.5 (D) wild type and (E) *Nos3$^{-/-}$* embryos. F: Cell lineage analysis at E12.5 also showed reduced contribution of NCC-derived cells within the ascending aorta of *Nos3$^{-/-}$* (N=4) embryos when compared to age matched wild type (N=4). Incomplete coverage of inner media by NCC-derived cells was observed in

the inner media in *Nos3*$^{-/-}$ of both E17.5 and E12.5 embryos (white arrowheads). G,H: 3D reconstruction of E12.5 (G) wild type *Wnt1Cre*$^{+}$ hearts showed NCC-derived cells (green) surrounding the complete lumen (red) of the ascending aorta. In contrast, to wild type, E12.5 (H) *Nos3*$^{-/-}$; *Wnt1Cre*$^{+}$;*mTmG* embryos showed a reduced number of NCCs throughout the ascending aorta as well as an incomplete NCC coverage of the aortic root and proximal ascending aorta. Colour coding: myocardium (transparent grey), parietal outflow tract cushion (purple), Non-coronary leaflet (yellow), septal outflow tract cushion (light blue), pulmonary trunk (dark blue). Nuclear DAPI staining: Blue, *: $P<0.05$. Ao: Aorta, R: right, L: left, V: Ventral, D: Dorsal. * P value <0.05 were determined by two tailed student T-test. Scale bars: 50µm. Data are mean ± s.d.

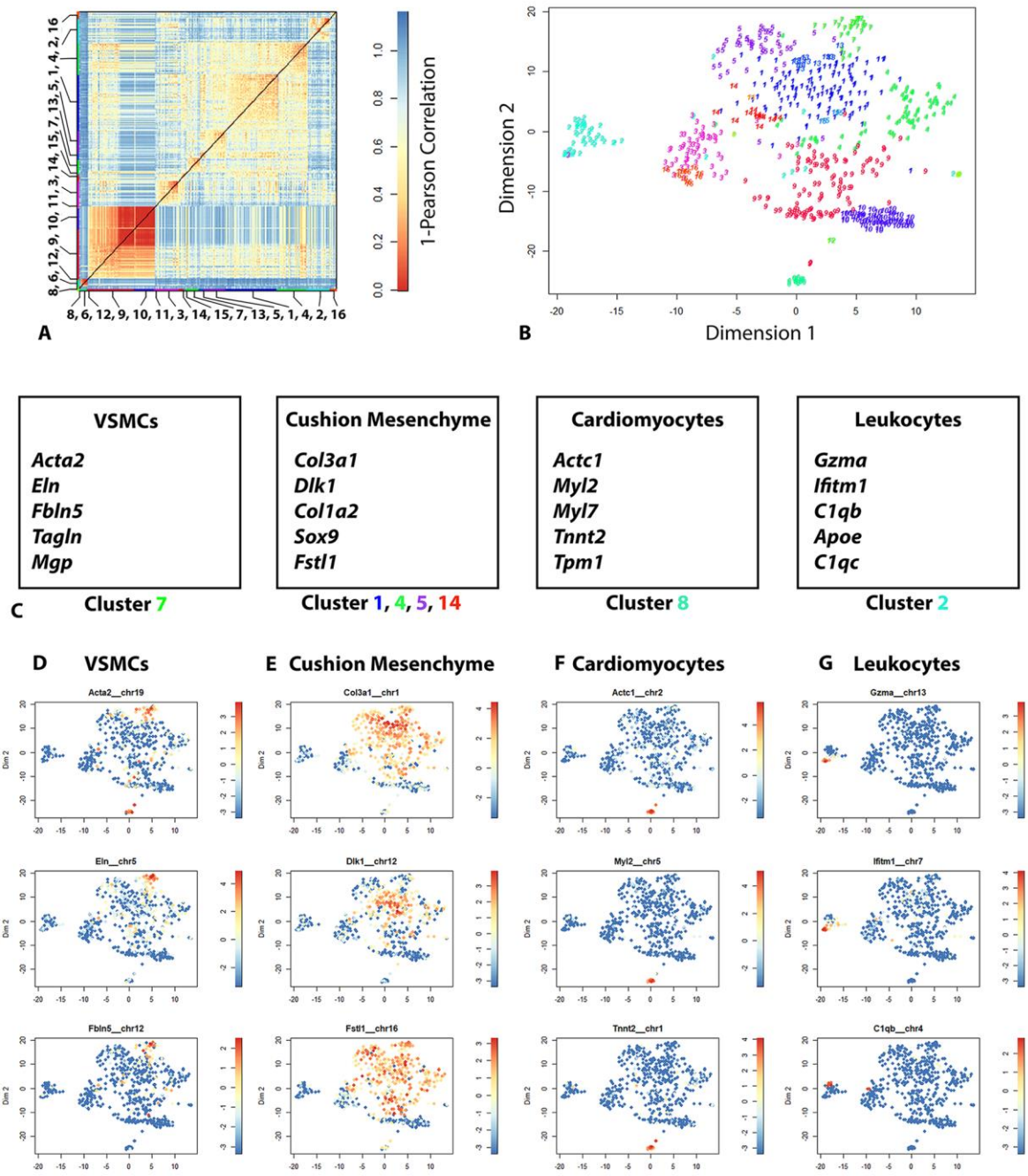

Figure 5. ***Clustering of cardiac outflow tract cells based on gene expression*****.**
A: Heatmap depicting distance in cell-to cell transcriptomes of 607 cells obtained from wild type outflow tract tissue at E12.5. K-medoids clustering identified 16 clusters. B: t-SNE map showing cell clusters based on affinity in RNA transcriptome profiles corresponding to different cell types. C: Tables of established marker genes used to identify cell types corresponding to cluster numbers indicated in B. D-G: t-SNE maps showing relative RNA expression of cell specific markers indicating (D) Vascular smooth muscle cells (VSMC), (E) Cushion mesenchyme, (F) Cardiomyocytes, (G) Leukocytes. Data are shown as normalized transcript counts on a colour-coded logarithmic scale.

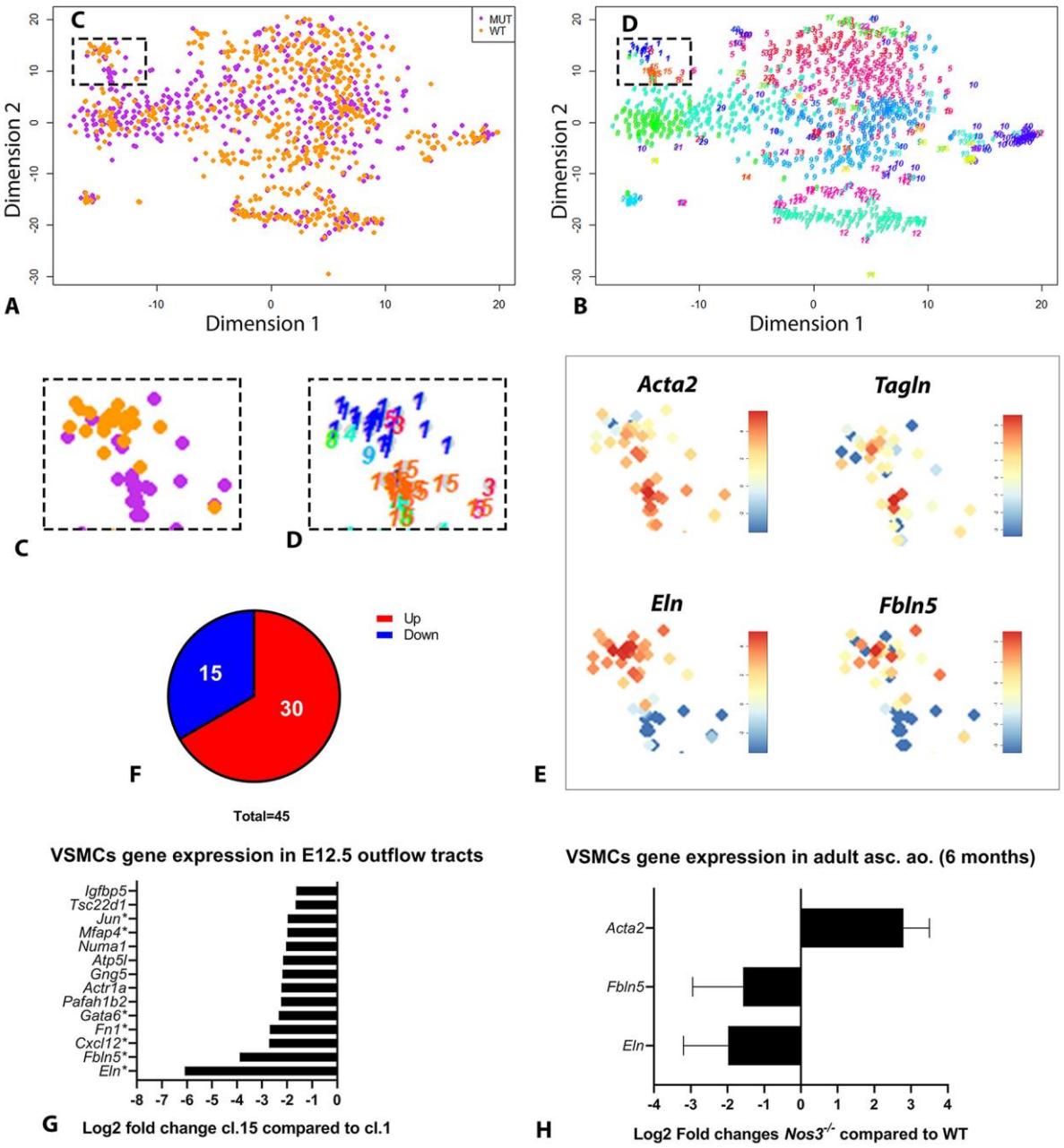

Figure 6. ***Single cell transcriptome analysis of WT and Nos3$^{-/-}$ mice.***

A-B: t-SNE map indicating transcriptome similarities among 1099 single cells. A: Colors highlight the genotype of cells (wild type: orange, *Nos3*$^{-/-}$: purple). B: Numbers highlight the cluster numbers identified. C-D: Enlargement of the t-SNE map from A and B, focussing on the vascular smooth muscle clusters (VSMCs) showing segregation of wild type and *Nos3*$^{-/-}$ VSMC cells. E: t-SNE maps showing relative RNA expression of VSMC clusters. F: Pie chart showing the number of significantly (P<0.05) up- and down regulated genes in *Nos3*$^{-/-}$ VSMCs *(cl.15)* compared to wild type VSMCs (cl.1) at E12.5. G: Expression of the 15

significantly downregulated genes in the *Nos3*$^{-/-}$ VSMC cluster (cl.15) compared to the VSMCs in the wild type cluster (cl.1). Known genes linked to aneurysm formation have been marked with an asterix (asterix).H: qPCR of top 3 differential genes found in E12.5 VSCMs by scRNA-seq in adult (P6 months) VSMCs from the ascending aorta (N=5) of wild type and *Nos3*$^{-/-}$ mice (N=5.). *Rpl32* was used as reference gene.

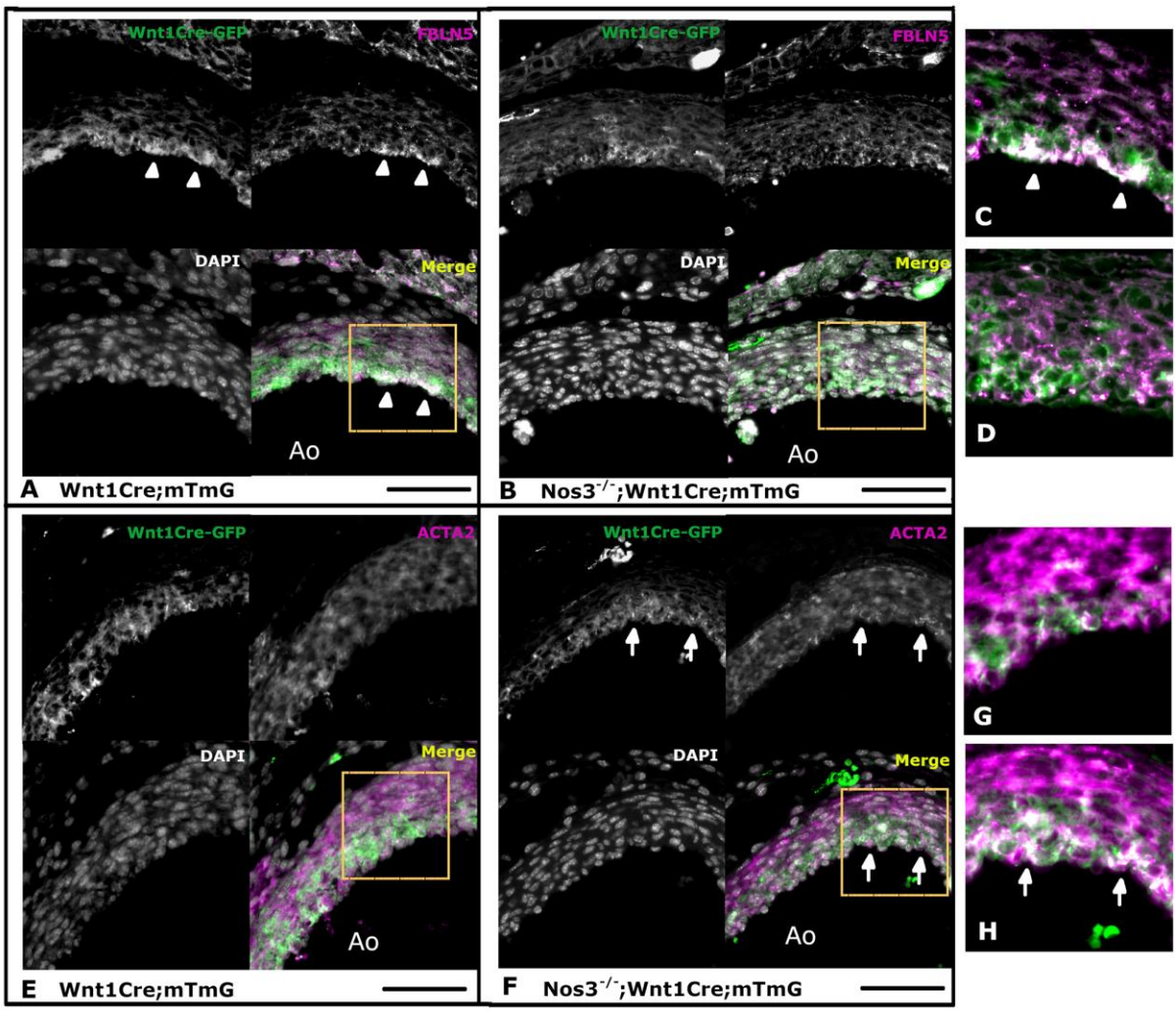

Figure 7. ***Genetic variations translate to misregulated protein expression in neural crest derived vascular smooth muscle cells of Nos3$^{-/-}$ embryos.***

Fluorescent microscopy images of transversal sections of the aortic vessel wall in *Wnt1Cre;mTmG* and *Nos3$^{-/-}$;Wnt1Cre;mTmG* embryos age E17.5. A: Neural crest derived vascular smooth muscle cells (VSMCs) (green), line the inner media of the aortic vessel wall and express FBLN5 (magenta) (see arrowheads). B: *Nos3$^{-/-}$* Neural crest derived VSMCs show reduced accumulation of FBLN5 compared to wild type embryos. C-D: Magnified view of the annotated area for Wnt1Cre-GFP and FBLN5 channels of A and B respectively. E-F: Neural crest derived VSMCs express ACTA2 (magenta) showing increased expression of ACTA2 in neural crest derived VSMCs in *Nos3$^{-/-}$* embryos (indicated by arrows). G-H: Enlarged view of the squared area for Wnt1Cre-GFP and ACTA2 channels of E and F respectively. Nuclear staining: DAPI (grey). Scale bars: 50µm, Ao: Aorta.

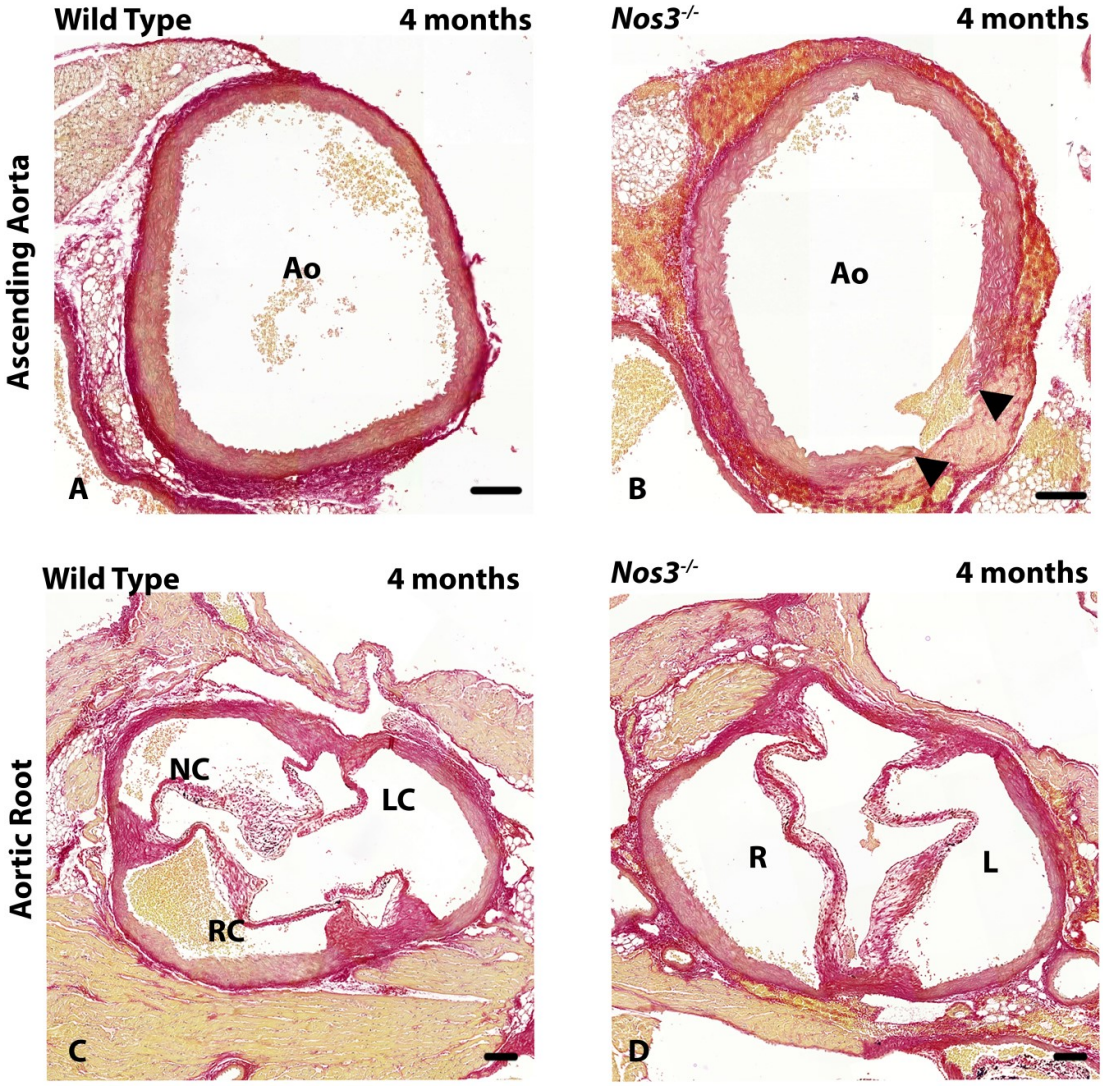

Fig. S1. Aortic dissection in Nos3$^{-/-}$ mice is associated with BAV.

Additional histological staining of wild type and *Nos3*$^{-/-}$ mice presented in figure 1 stained with a combination of collagen (red) and elastin (pink) showing the ascending aorta (A-B) and aortic root (C-D). This case of aortic dissection developed in conjunction with a bicuspid aortic valve (D). Aortic dissection is apparent in the aortic vessel wall of the *Nos3*$^{-/-}$ mouse (arrow heads). Ao: Aorta, NC: Non-coronary leaflet, RC: Right coronary leaflet, LC: Left coronary leaflet, R: Right leaflet, L: Left leaflet, Scale bar: 100 µm

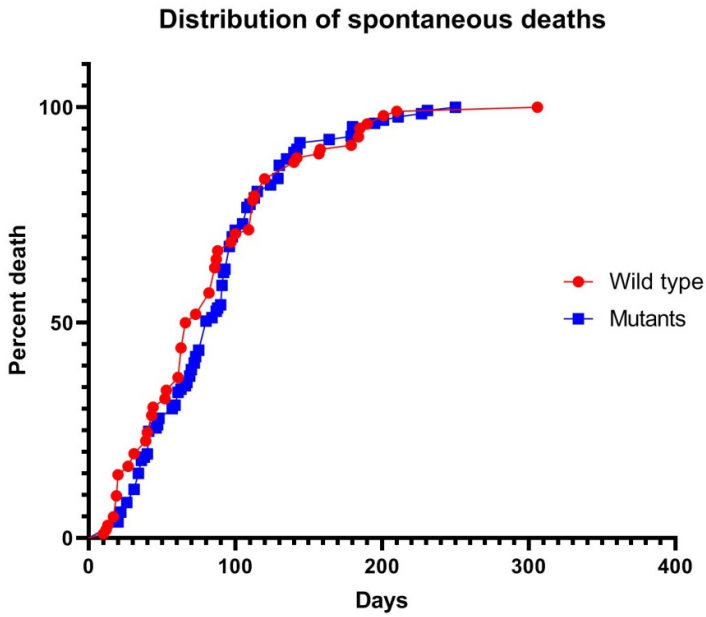

Fig. S2. Temporal distribution of spontaneous death events.
Wild type (n=103) and *Nos3*$^{-/-}$ (n=133) in which spontaneous death was observed were examined for the chronologic distribution of death events. No significant (P >0.05) difference was observed between wild type and mutant populations using Mantel-Cox comparison of survival curves.

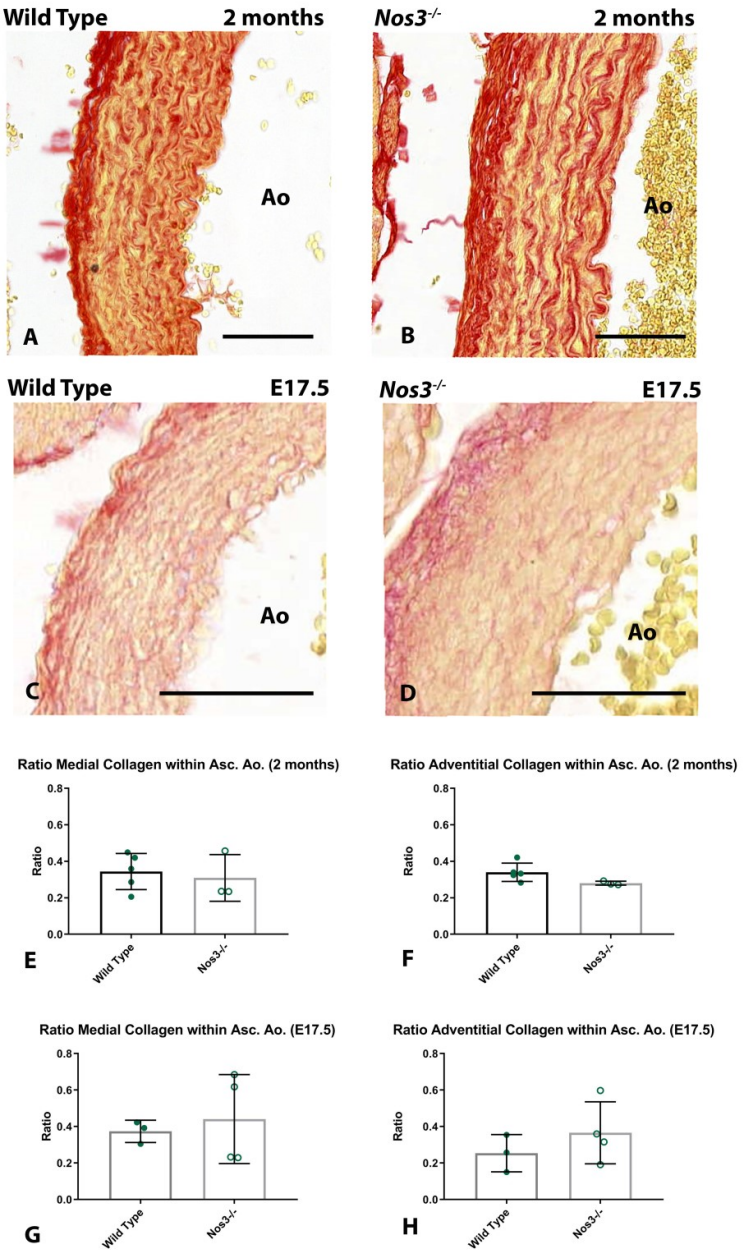

Fig. S3. Collagen deposition is not affected in the ascending aortic wall of Nos3$^{-/-}$ mice. A-B: Transverse sections of the aortic wall of adult (A) wild type and (B) *Nos3*$^{-/-}$ mice stained with Sirius red to show collagen deposition in the media and adventitia of the ascending aorta. C-D: Sirius red staining of the embryonic aortic wall of (C) wild type and (D) *Nos3*$^{-/-}$ mice at stage E17.5. E-H: Volumetric quantification of collagen staining within the medial (E,G) as well as adventitial layers (F,H) of the adult and embryonic ascending aortic wall show no difference ($P > 0.05$) in the deposition of collagen between wild type and *Nos3*$^{-/-}$ mice. Ao: Aorta. Data are mean ± s.d. for $n \geq 3$ mice per group. Scale bar: 50 µm

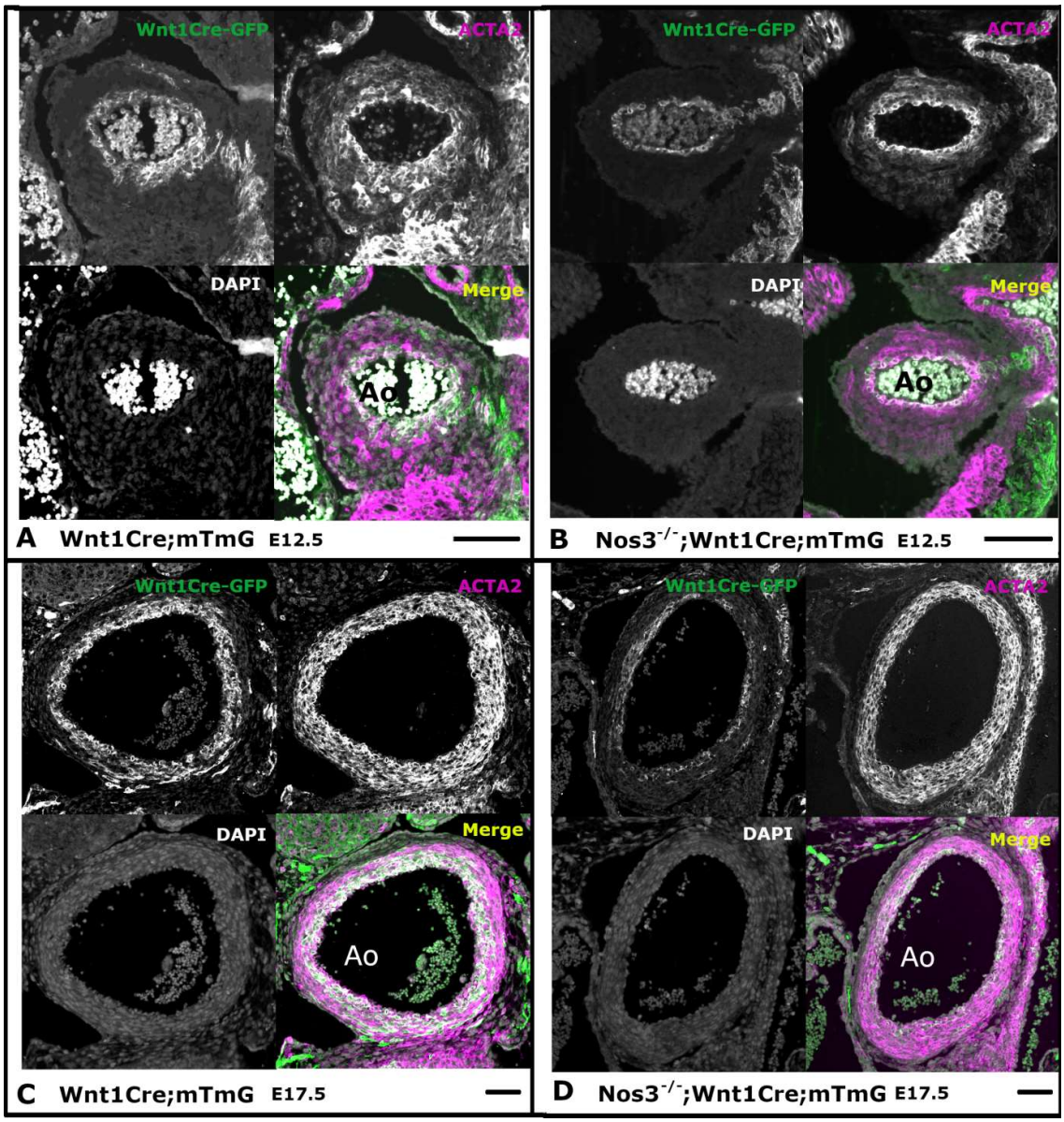

Fig. S4. Neural crest derived smooth muscle cells populate the inner media of tthe ascending aortic vessel wall.

A-B: Transversal sections of the e a ascending aorta of Wnt1Cre;mTmG and *Nos3*$^{-/--}$ *;Wnt1Cre;mTmG* embryos at E12E12.5. Neural crest derived vascular smooth muscclle cells (VSMCs) express both Wnt1Cree-GFP (green) and ACTA2 (magenta). C-D: Fluoruorescent images similar to A and B, but shs howing embryos of developmental age E17.5. NNote that expression of ACTA2 is more pronounpronounced in neural crest derived VSMCs than VVSMCs of different origin at E12.5 in both w wild type and *Nos3*$^{-/-}$ embryos. Nuclear staining:ng: DAPI (grey). Scale bars: 50µm. Ao: AorA orta.

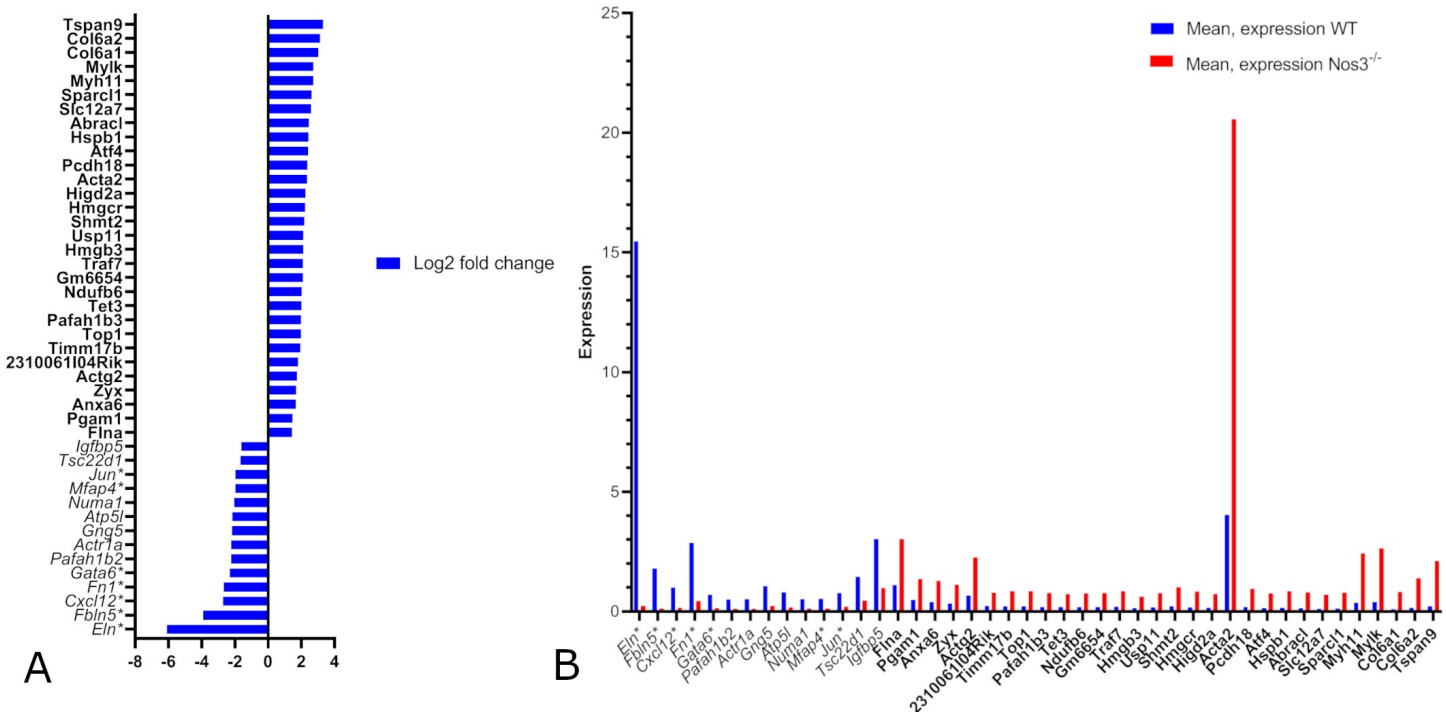

Fig. S5. Differential gene expression profiles among VSMC clusters.
A-B: The differential expression profile of VSMCs affected by the *Nos3* mutation. Astrix indicates downregulated genes associated with aneurysm formation. Bold gene names correspond to upregulated genes.

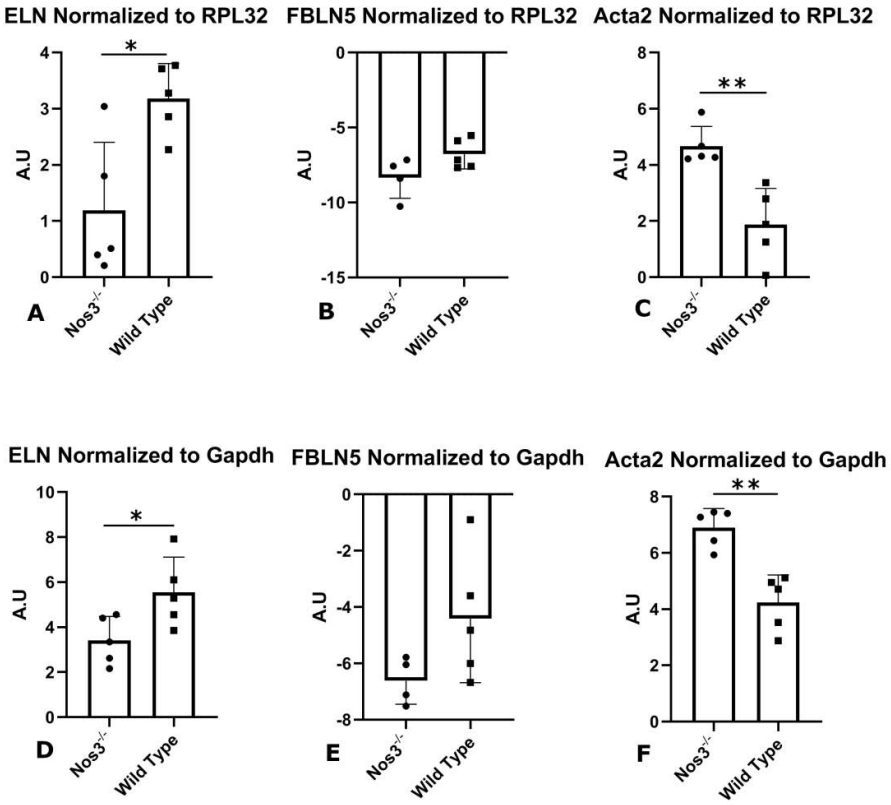

Fig. S6. Extended qPCR evaluatation normalized to Rpl32 and Gapdh.
A-F: qPCR expression results of 6 month old wild type (N=5) and *Nos3*$^{-/-}$ (N=5) mice using *Rpl32* as well as *Gapdh* as reference genes. Statistical analysis were performed using a two-tailed student T-test, * and ** indicate P<0.05 and P<0.01 respectively. A.U: Arbitrary Units. Data are mean ± sd.

ELN_FWD	CCC ACC TCT TTG TGT TTC GC
ELN_REV	CCC AAA GAG CAC ACC AAC AAT
FBLN5_FWD	GTG CTT GGG GTT GGT TTT GA
FBLN5_REV	TCA GTT CCC CAT CTT TTG CCA
ACTA2_FWD	GCT ACG AAC TGC CTG ACG G
ACTA2_REV	TAG GTG GTT TCG TGG ATG CC
RPL32_FWD	CAC CAC TCA GAC CGA TAT GTG AAA A
RPL32_REV	TGT TGT CAA TGC CTC TGG GTT T
GAPDH_FWD	TTG ATG GCA ACA ATC TCC AC
GAPDH_REV	CGT CCC GTA GAC AAA ATG GT

Table S1. Primers used for qPCR